

1 **A fifteen year record of CO emissions constrained by MOPITT CO**
2 **observations**

4 Zhe Jiang^{1,2}, John R. Worden¹, Helen Worden², Merritt Deeter², Dylan B. A. Jones³, Avelino F.
5 Arellano⁴, Daven K. Henze⁵

8 ¹Jet Propulsion Laboratory, California Institute of Technology, Pasadena, CA, USA

9 ²National Center for Atmospheric Research, Boulder, CO, USA

10 ³Department of Physics, University of Toronto, Toronto, ON, Canada

11 ⁴Department of Hydrology and Atmospheric Sciences, University of Arizona, Tucson, AZ, USA

12 ⁵Department of Mechanical Engineering, University of Colorado, Boulder, CO, USA

13

14

15

16

17

18

19

20

21

22

23

24

25

26

27

28

29 **Abstract**

30 Long-term measurements from satellites and surface stations have demonstrated a
31 decreasing trend of tropospheric carbon monoxide (CO) in the Northern Hemisphere over the past
32 decade. Likely explanations for this decrease include changes in anthropogenic, fires, and/or
33 biogenic emissions or changes in the primary chemical sink hydroxyl radical (OH). Using
34 remotely sensed CO measurements from the Measurement of Pollution in the Troposphere
35 (MOPITT) satellite instrument, in-situ methyl chloroform (MCF) measurements from World Data
36 Centre for Greenhouse Gases (WDCGG), and the adjoint of the GEOS-Chem model, we estimate
37 the change in global CO emissions from 2001-2015. We show that the loss rate of MCF varies by
38 0.2% in the past 15 years, indicating that changes in global OH distributions do not explain the
39 recent decrease in CO. Our two-step inversion approach for estimating CO emissions is intended
40 to mitigate the effect of bias errors in the MOPITT data as well as model errors in transport and
41 chemistry, which are the primary uncertainties when quantifying CO emissions using these
42 remotely sensed data. Our results confirm that the decreasing trend of tropospheric CO in the
43 Northern Hemisphere is due to decreasing CO emissions from anthropogenic and biomass burning
44 sources. In particular, we find decreasing CO emissions from the United States and China in the
45 past 15 years, unchanged anthropogenic CO emissions from Europe since 2008. We find
46 decreasing trends of biomass burning CO emissions from boreal North America, boreal Asia and
47 South America, but little change over Africa. In contrast to prior results we find positive trend in
48 CO emissions is likely for India and southeast Asia.

49

50 **1. Introduction**

51 Tropospheric CO is a product of incomplete combustion and a byproduct of the oxidation

52 of hydrocarbons. It plays a key role in atmospheric chemistry because it is the main sink for OH,
53 and an important precursor for tropospheric ozone (O_3). Recent studies demonstrated significant
54 change in tropospheric CO abundance in the past decade. Using Atmospheric Infrared Sounder
55 (AIRS) CO measurements, Warner et al. (2013) indicated that Northern Hemispheric CO mixing
56 ratio decreased by 1.28 ppb/year in the period of 2003-2012. Worden et al. (2013) demonstrated
57 Northern Hemispheric CO column measurements from MOPITT show a decrease of ~0.92%/year
58 in the period of 2000-2011. Using observations from Mt. Bachelor Observatory, Gratz et al. (2015)
59 also show a negative trend of CO concentration by 1.9%/year in the period of 2004-2013.
60 However, the reason for the large variation of tropospheric CO abundance is still unclear; for
61 example, Strode et al. (2016) found decreases in modeled CO abundance over North America and
62 Europe, but increases over China, based on bottom-up emissions.

63 There is currently much effort focused on accurately quantifying emissions of CO. For
64 fossil fuels and biofuels, energy consumption statistics and emission factors are usually used to
65 construct the emission inventories (e.g. Streets et al. 2006; Ohara et al. 2007; Zhang et al. 2009;
66 Zhao et al. 2012). Biomass burning emissions are commonly calculated as the product of burned
67 area, fuel loads, combustion completeness and emission factors (e.g. van der Werf et al. 2006,
68 2010; van Leeuwen and van der Werf 2011). Because of the large uncertainties in the emission
69 inventories, space-based remotely sensed measurements and surface/aircraft in-situ observations
70 have been assimilated to provide “top-down” constraints on CO emissions (e.g., Arellano et al.,
71 2006; Chevallier et al. 2009; Jones et al., 2009; Kopacz et al., 2010; Jiang et al., 2011; Fortems-
72 Cheiney et al. 2011; Hooghiemstra et al. 2012; Miyazaki et al. 2015). In a recent study, Yin et al.
73 (2015) constrained global CO emissions for the period 2002-2011 to investigate the possible
74 reasons for the decreasing CO abundance in the Northern Hemisphere. Using MOPITT column

75 data (version 6J) over the whole globe, Yin et al. (2015) indicate that the negative trend in the
76 Northern Hemisphere is driven by decreasing anthropogenic emissions from North America,
77 Europe and China.

78 The major sink of tropospheric CO is OH. Because of its high variability and short lifetime
79 (about one second), it is difficult to assess the spatial and temporal variation of global OH through
80 direct measurements (Spivakovskiy et al. 2000; Lelieveld et al. 2004). Alternatively, Montzka et
81 al. (2011) demonstrated small interannual variability of global OH for the period 1997-2007 by
82 using the loss rate of MCF as a proxy. The measurements of MCF are assimilated in recent CO
83 inversion studies to provide updated OH (e.g. Fortems-Cheiney et al. 2011, 2012; Yin et al. 2015),
84 but the estimates are adversely affected by the sparse distribution of measurements.

85 The objective of this work is to investigate the dominant reasons for the decreasing CO
86 trend in the Northern Hemisphere, and to provide updated CO emission estimates for model studies.
87 Using methods and results from our prior work, our approach for estimating emissions is intended
88 to reduce the effects of model errors of transport and chemistry, as well as bias errors in the data,
89 on our conclusions about CO emissions; these are the primary uncertainties that affect CO
90 emissions estimates. For example, bias errors as a function of latitude in MOPITT data can have a
91 substantial impact on emissions estimates (Deeter et al., 2014). Model errors of transport and
92 chemistry will have variable and substantial effects on CO emissions in different parts of the globe
93 due to seasonal and latitudinal variations in convection, advection, and boundary layer height
94 (Jiang et al., 2013, 2015a, 2015b).

95 In order to reduce the influences from these measurement and model transport systematic
96 errors, we performed a two-step inversion by combining sequential Kalman Filter (Jiang et al.
97 2013, 2015a, 2015b) with four-dimensional variational (4D-Var) assimilation (Henze et al. 2007)

98 in this work, using the GEOS-Chem model. Instead of optimizing the CO concentrations and
99 emissions simultaneously (e.g. Fortems-Cheiney et al. 2011, 2012; Yin et al. 2015), our first step,
100 the sequential Kalman Filter, modifies the atmospheric CO concentration directly to provide low
101 bias initial (monthly) and boundary (hourly) conditions, whereas the second step (4D-Var)
102 constrains CO emissions assuming perfect initial and boundary conditions. We also apply bias
103 corrections to MOPITT and compare the surface CO concentrations obtained by constraining the
104 model with either MOPITT profile, total column, or lower troposphere data to test which data type
105 provides the most accurate comparison with independent surface in-situ measurements.

106 This paper is organized as follows: in Section 2 we describe the MOPITT instruments and
107 the GEOS-Chem model used in this work. In Section 3 we outline the inverse method. We then
108 investigate the long-term variations of global tropospheric OH and CO emissions in Section 4, and
109 we discuss the changes in tropospheric CO, and the contributions from emissions and
110 meteorological conditions. Our conclusions follow in Section 5.

111 **2. Observations and Model**

112 **2.1. MOPITT**

113 The MOPITT instrument was launched on December 18, 1999 on the NASA/Terra
114 spacecraft. The satellite is in a sun-synchronous polar orbit of 705 km and crosses the equator at
115 10:30 local time. The instrument makes measurements in a 612 km cross-track scan with a
116 footprint of 22 km x 22 km, and provides global coverage every three days. The MOPITT data
117 used here were obtained from the joint (J) retrieval (V6J) of CO from TIR (4.7 μ m) and NIR (2.3 μ m)
118 radiances using an optimal estimation approach (Worden et al., 2010; Deeter et al., 2011). The
119 retrieved volume mixing ratios (VMR) are reported as layer averages of 10 pressure levels (surface,
120 900, 800, 700, 600, 500, 400, 300, 200 and 100 hPa). The relationship between the retrieved CO

121 profile and the true atmospheric state can be described as:

122
$$\hat{z} = z_a + A(z - z_a) + G\epsilon \quad (1)$$

123 where z_a is the MOPITT a priori CO profile, z is the true atmospheric state, $G\epsilon$ describes the
124 retrieval error, and $A = \partial\hat{z}/\partial z$ is the MOPITT averaging kernel matrix, which gives the sensitivity
125 of the retrieval to the actual CO in the atmosphere. The MOPITT V6 data have been evaluated by
126 Deeter et al. (2014) using aircraft measurements from HIAPER Pole-to-Pole Observations (HIPPO)
127 and the National Oceanic and Atmospheric Administration (NOAA). For the TIR/NIR multi-
128 spectral retrievals, they found negative bias drift (-1.27%/year) at lower troposphere (800 hPa),
129 and positive bias drift (1.64%/year) at upper troposphere (200 hPa). The bias drift in the total
130 column is negligible (0.003%/year). Following our previous studies (Jiang et al. 2013; 2015a;
131 2015b), we reject MOPITT data with CO column amounts less than 5×10^{17} molec/cm² and with
132 low cloud observations. The threshold of 5×10^{17} molec/cm² was selected to prevent unrealistically
133 low CO columns from adversely impacting the inversion analyses. Since the NIR radiances
134 measure reflected solar radiation, only daytime data are considered here.

135 Figure 1 shows the comparison between MOPITT CO retrievals and HIPPO aircraft
136 measurements. The aircraft measurements are smoothed with MOPITT averaging kernels. The
137 comparison demonstrates a negative bias of MOPITT CO retrievals in the tropics and a positive
138 bias at the middle latitudes in the lower troposphere. Opposite bias is observed in the upper
139 troposphere. Similar latitude dependent biases in remote sensing retrievals have been revealed for
140 methane (CH₄) observations from Scanning Imaging Absorption Spectrometer for Atmospheric
141 Chartography (SCIAMACHY, Bergamaschi et al. 2007, 2009; Meirink et al. 2008), Greenhouse
142 Gases Observing Satellite (GOSAT, Turner et al. 2015), and CO observation from MOPITT
143 (version 4, Hooghiemstra et al. 2012). Similar to previous studies, we reduce the adverse effect of

144 the latitude dependent bias by applying latitude dependent correction factors to MOPITT CO
145 retrievals, based on the black solid line in Figure 1, which represents a 4-order polynomial curve
146 fitting (in a least-squares sense) for all data points. It should be noted that the possible seasonal
147 variations of MOPITT retrieval biases are not included in our analysis because we are focusing on
148 the interannual variation of CO emissions.

149 **2.2. GEOS-Chem**

150 The GEOS-Chem global chemical transport model (CTM) [www.geos-chem.org] is driven
151 by assimilated meteorological fields from the NASA Goddard Earth Observing System (GEOS-5)
152 at the Global Modeling and data Assimilation Office. For the simulations in this work, various
153 versions of GEOS meteorological fields are used, including GEOS-4 (2000-2003), GEOS-5 (2004-
154 2012) and GEOS-FP (2013-2015). We use version v35j of the GEOS-Chem adjoint, which is based
155 on v8-02-01 of the forward GEOS-Chem model, with relevant updates through v9-02-01. Our
156 analysis is conducted at a horizontal resolution of $4^{\circ} \times 5^{\circ}$ with 47 vertical levels and employs the
157 CO-only simulation in GEOS-Chem, which uses archived monthly OH fields from the full
158 chemistry simulation. The OH fields used in this work are from GEOS-Chem version v5-07-08,
159 with a global annual mean OH concentration of 0.99×10^6 molec/cm³ (Evans et al. 2005). The
160 potential long-term variation of global tropospheric OH is evaluated in section 4.

161 The global anthropogenic emission inventory is from EDGAR 3.2FT2000 (Olivier et al.,
162 2001), but are replaced by the following regional emission inventories: the US Environmental
163 Protection Agency National Emission Inventory (NEI) for 2008 in North America, the Criteria Air
164 Contaminants (CAC) inventory for Canada, the Big Bend Regional Aerosol and Visibility
165 Observational (BRAVO) Study Emissions Inventory for Mexico (Kuhns et al. 2003), the
166 Cooperative Program for Monitoring and Evaluation of the Long-range Transmission of Air

167 Pollutants in Europe (EMEP) inventory for Europe in 2000 (Vestreng et al. 2002) and the INTEX-
168 B Asia emissions inventory for 2006 (Zhang et al. 2009). Biomass burning emissions are based on
169 the Global Fire Emission Database (GFED3, van der Werf et al. 2010). The a priori biomass
170 burning emissions in Sep-Nov 2006 were applied to Sep-Nov 2015 over Indonesia. Additional CO
171 sources come from oxidation of methane and biogenic volatile organic compounds (VOCs) as
172 described in previous studies (Kopacz et al. 2010; Jiang et al. 2013). The biogenic emissions are
173 simulated using the Model of Emissions of Gases and Aerosols from Nature, version 2.0
174 (MEGANv2.0, Guenther et al. 2006). The distribution of the annual mean CO emissions for 2001-
175 2015 is shown in Figure 2. The annual global sources are 892 Tg CO from fossil fuel, biofuel and
176 biomass burning, 623 Tg CO from the oxidation of biogenic VOCs, and 876 Tg CO from the
177 oxidation of CH₄.

178 **3. Inversion Approach**

179 We use the 4D-var data assimilation system in GEOS-Chem (Henze et al. 2007) to
180 constrain the CO sources. In this approach, we minimize the cost function defined as:

$$181 J(x) = \sum_{i=1}^N (F_i(x) - z_i)^T S_{\Sigma}^{-1} (F_i(x) - z_i) + (x - x_a)^T S_a^{-1} (x - x_a) \quad (2)$$

182 where x is the state vector of CO emissions, N is the number of MOPITT observations that are
183 distributed in time over the assimilation period, z_i is a given MOPITT measurement, and $F(x)$ is
184 the forward model. The temporal resolution of forward model output ($F(x)$) is one hour, and
185 consequently, the high resolution MOPITT measurements are averaged temporally (one-hour
186 resolution) and spatially (4°x5° resolution) to produce grid mean observations. The number (N) of
187 grid mean observations in our assimilation window (one month) is around 10000.

188 The error estimates are assumed to be Gaussian, and are given by S_{Σ} , the observational
189 error covariance matrix, and S_a , the a priori error covariance matrix, respectively. The Gaussian

190 assumption excludes important systematic errors, such as biases in OH distribution, long-range
191 transport and satellite retrievals in the cost function. Due to lack of meaningful information about
192 the systematic errors, we assume a uniform observation error of 20% without spatial correlation.
193 The combustion CO sources (fossil fuel, biofuel and biomass burning) and the oxidation source
194 from biogenic VOCs are combined together, assuming a 50% uniform a priori error. We optimize
195 the source of CO from the oxidation of CH₄ separately as an aggregated global source, assuming
196 an a priori uncertainty of 25%.

197 Without consideration of systematic errors, the a posteriori error covariance matrix is the
198 inverse of the Hessian matrix, which is not stored in the 4D-var optimization scheme. Bousserez
199 et al. (2015) presented an approach to construct the a posteriori error covariance matrix using the
200 approximation of Hessian matrix. As opposed to earlier studies using surface measurements, the
201 high spatial density of measurements from satellite instruments can effectively suppress the
202 contribution from random errors in the cost function, leaving systematic errors as the critical factor
203 in the uncertainty. As shown by Heald et al. (2004), different assumptions about the inversion
204 configuration (systematic errors) can produce differences in the source estimates that are
205 significantly larger than the a posteriori errors calculated based on random errors. Consequently,
206 estimates of a posteriori uncertainties are not provided in this work (e.g. Table 1 and Table 2).

207 Removing the bias in initial conditions is essential for inverse analysis (Jiang et al. 2013),
208 and can be performed with various data assimilation techniques. Model simulations driven by
209 optimized emissions can provide good initial conditions (e.g. Gonzi et al. 2011; Bruhwiler et al.
210 2014; Deng et al. 2014; Houweling et al. 2014). Alternatively, tracer concentrations can be
211 modified directly to avoid the effect from long-range transport error (e.g. Kopacz et al. 2009; Jiang
212 et al. 2013, 2015a). There are also efforts to optimize emissions and concentrations simultaneously

213 (e.g. Fortems-Cheiney et al. 2011, 2012; Bergamaschi et al. 2013; Yin et al. 2015), however, the
214 contributions from emissions and concentrations to model bias may be hard to be distinguished.
215 Figure 3 shows the methodology of our assimilation system. Following our previous studies (Jiang
216 et al. 2013, 2015a, 2015b), we produce initial conditions at the beginning of each monthly
217 assimilation window by assimilating MOPITT data using a sequential Kalman filter. For the results
218 presented here, the Kalman filter assimilation was carried out from March 1, 2000 to December
219 31, 2015.

220 Systematic errors have critical influences on inverse analysis. Jiang et al. (2013) found that
221 the modeled CO concentration from a 10-day forecast simulation have large discrepancy with
222 assimilated CO fields, because of bias in model convective transport. Jiang et al. (2015a)
223 demonstrated that free tropospheric CO is more susceptible to the influences of OH bias than lower
224 tropospheric CO due to the process of long-range transport. Previous studies suggest the influences
225 of systematic errors can be mitigated by enhancing the contributions from local emissions to the
226 discrepancy between model and data, while keeping the influence from long-range transport as
227 low as possible due to sources of uncertainties that are difficult to quantify. For example, Pifster
228 et al. (2005) constrained biomass burning CO emissions from boreal North America with
229 optimized CO fields outside the impacted region; Jiang et al. (2015b) indicated that the results of
230 regional inversions are more reliable when the boundary conditions are optimized.

231 In this work, we designed a two-step inversion to reduce the effects of these systematic
232 errors. As shown in Figure 3, we define the ocean scene (red grids) as boundary conditions. In the
233 first step of our inverse analysis, sequential Kalman filter assimilation, we directly modify CO
234 concentrations without any change to emissions in order to provide an optimized CO fields as
235 consistent as possible with MOPITT. In the second step, the optimized CO fields are used to

236 rewrite CO concentrations over the ocean every hour, while 4D-var inversion is employed to
237 constrain CO emissions, without any change on CO distribution over ocean. Only MOPITT data
238 over land (white grids) were assimilated to constrain CO emissions in the second step. With the
239 fixed/optimized boundary conditions, the global inversion system has been converted to a
240 combination of several regional inversions. Consequently, the emission and transport errors from
241 one continent (e.g. North America) will not affect the emission estimation of another continent
242 (e.g. Europe).

243 **4. Results and Discussion**

244 **4.1. Long-term variation of global tropospheric OH**

245 The distribution of tropospheric OH has significant influence on the inverse analysis of CO
246 emissions (Jiang et al. 2011). Various approaches have been employed to improve the OH
247 distribution in previous studies. Jiang et al. (2013) assimilated MOPITT CO retrievals in full
248 chemistry model simulation to provide updated OH fields. Miyazaki et al. (2015) demonstrated
249 that assimilation of Tropospheric Emission Spectrometer (TES) O₃, Ozone Monitoring Instrument
250 (OMI) NO₂, and MOPITT CO can provide a better description of tropospheric OH. There are also
251 recent efforts that have assimilated surface in-situ MCF measurements (Fortems-Cheiney et al.
252 2011, 2012; Yin et al. 2015). However, because of the uncertainties in model chemistry schemes,
253 potential bias drifts in satellite remotely sensed observation, and sparse distribution of surface in-
254 situ measurements, OH abundances provided by these approaches may not be ideal for the
255 estimation of long-term CO variation.

256 Emissions of MCF are regulated by the Montreal Protocol agreement. The loss rate of MCF
257 has become a good tool to evaluate the variation of tropospheric OH (e.g. Krol et al. 1998;
258 Bousquet et al. 2005; Prinn et al. 2005; Montzka et al. 2011). Using the same approach as Montzka

259 et al. (2011), we assess the variation of tropospheric OH in the period of 2001-2015. Figure 4a
260 shows the locations of WDCGG sites with MCF measurements, and Figure 4b shows the global
261 mean MCF concentration in the past 15 years. Similar as Montzka et al. (2011), our result shows
262 a exponential decrease of MCF concentration. The loss rate of MCF, derived from 12-month apart
263 of monthly means [e.g., $\ln(MCF_{Jan2007}/MCF_{Jan2006})$] varies by 0.2% in the past 15 years (Figure
264 4c). The interannual variation is more likely due to the sparsity and discontinuity of measurements.

265 The small variation of loss rate of MCF demonstrates that the long-term variation of global
266 mean OH distributions is negligible in the past 15 years. Consequently, the decreasing trend of
267 tropospheric CO in North Hemisphere is driven by decreasing CO sources, rather than sinks. For
268 this reason, the default monthly OH fields of GEOS-Chem model (Evans et al. 2005), without
269 interannual variability, are used in this work to constrain the long-term variation of CO emissions.
270 Because the abundances of tropospheric OH have large regional discrepancies (e.g. Jiang et al.
271 2015a), it is possible that the actual OH is more variable at regions lacking MCF measurements
272 (e.g. India and southeast Asia). Futhermore, the magnitude and seasonality of the default monthly
273 OH fields could also have uncertainty. Consequently, the magnitude of CO emissions in our
274 analysis may still be affected by biases in OH, although the two-step assimilation system is
275 designed to suppress their influence.

276 **4.2. Long-term variation of global CO emissions**

277 In this work, we performed monthly inversions for the period of 2001-2015, using
278 MOPITT column, profile and lower tropospheric profile (lowest three retrieval levels) data to
279 investigate the influences associated with vertical sensitivity of satellite instrument and model
280 transport error. Figure 5 shows the CO emission trends for 2001-2015 constrained by these
281 different datasets. Because of the combination of various emission categories (i.e. anthropogenic,

282 biomass burning and VOC oxidation) in our methodology, we cannot completely separate the a
283 posteriori emission estimates from different sources. However, the various spatial and temporal
284 distribution of emissions sources (e.g. anthropogenic vs. biomass burning) provides valuable
285 information to distinguish the contribution from each category. In order to further isolate the
286 influences of biomass burning, the months dominated by biomass burning (biomass burning CO >
287 50% of total CO emission in an individual grid) are excluded in the trend analysis for
288 anthropogenic and VOC sources (Figure 5).

289 For anthropogenic sources, all three analysis show significant emission reduction from
290 North America, Europe and China. The emission estimates constrained with MOPITT column and
291 profile data suggest increasing CO emissions from India and Southeast Asia. Conversely, the
292 emission estimate constrained with MOPITT lower tropospheric profile data shows a decreasing
293 trend in this region, and this decreasing trend is also obtained by Yin et al. (2015). As shown in
294 Jiang et al., (2013), errors in model convection in this region have a large effect on CO emissions
295 estimates, and information about the vertical profile of CO has a stronger influence on the results.

296 For biomass burning sources, we found a negative trend over boreal North America, boreal
297 Asia and South America, and a positive trend over Indonesia that is primarily due to the strong
298 impacts of El Nino in 2006 and 2015 on biomass burning in this region (e.g. Field et al., 2016).
299 Our results for biogenic VOCs are inconclusive; the emission estimates constrained with MOPITT
300 column and profile data show moderate positive trends in the tropics, and slight negative trends in
301 mid-latitude regions, whereas the emission estimate constrained with MOPITT lower tropospheric
302 profile data shows a negative trend globally.

303 **4.2.1. Regional analysis for anthropogenic emissions**

304 Figure 6a shows the regional variation of anthropogenic emissions from the United States

305 (US). The emission estimates constrained with MOPITT column and profile data match very well
306 with the a priori emissions, whereas the emission estimate constrained with MOPITT lower
307 tropospheric profile data is much higher. All three analyses demonstrate a significant emission
308 reduction over our study period. As shown in Table 1, the total anthropogenic CO emission
309 (constrained with MOPITT profile data) from US is 56.8 Tg in 2015, which is 35% lower than that
310 in 2001 (87.7 Tg). Figure 7a shows the monthly mean CO concentrations from WDCGG stations
311 in US, which demonstrates a similar decreasing trend as our analysis. The initial increase at 2001-
312 2002 could be caused by uncertainties in the data. The decreasing trend is consistent with the US
313 Environmental Protection Agency (EPA) Emissions Trends Data (<https://www.epa.gov/air-emissions-inventories/air-pollutant-emissions-trends-data>), and other observation records for
314 western US (Gratz et al. 2015), southeast US (Hidy et al. 2014) and North Atlantic (Kumar et al.
315 2013).
316

317 Figure 6b shows the regional variation of anthropogenic emissions from Europe. All three
318 analyses show an underestimation of a priori emissions, suggesting the CO emissions in the EMEP
319 inventory are too low. Our results show that anthropogenic emissions decrease during the period
320 of 2001-2007, but are almost unchanged in the following years, which is consistent with the
321 observations from WDCGG stations (Figure 7b). Recent studies (Hilboll et al. 2013; Schneider et
322 al. 2015) showed that NO₂ over Europe from SCIAMACHY is decreasing in the period of 2002-
323 2008, and almost unchanged in the period of 2008-2011. Henschel et al. (2015) indicated that the
324 unchanged NO₂ over Europe could be caused by European emissions that are failing to achieve
325 the expected reduction standards. Because anthropogenic CO and NO₂ share some of the same
326 combustion sources, it is possible that the unchanged CO emission in our analysis is also due to a
327 failure of emission controls.

328 Figure 6c shows the regional variation of anthropogenic emissions from east China. We
329 found Chinese anthropogenic emissions are increasing in the period of 2001-2004. Accompanied
330 with the global economy recession, the total anthropogenic CO emission (constrained with
331 MOPITT profile data) from east China decreases to 175.4 Tg in 2008, which is 15% lower than
332 that in 2004 (205.6 Tg). Our analysis shows a temporary increase of Chinese emissions in 2009
333 (185.9 Tg), followed by continuous decrease. The total Chinese anthropogenic CO emission is
334 159.0 Tg in 2015, which is 7% lower than that in 2001 (170.4 Tg). Using surface in-situ
335 measurements at Hateruma Island, Tohjima et al. (2014) constrained CO emissions from China
336 for the period 1999-2010. They found Chinese CO emission increases from 1999-2004, and
337 decreases since 2005. Using a “bottom-up” approach, recent studies (Zhao et al. 2012; Xia et al.
338 2016) indicated that the growth trend of Chinese CO emissions has been changed since 2005
339 because of improvements in energy efficiency and emission control regulations (e.g. Liu et al.
340 2015). Figure 7c shows the observation records from 2 stations in the East China outflow region,
341 which demonstrate similar variations.

342 Figures 6d-6e show the regional variation of anthropogenic emissions from India and
343 Southeast Asia. The emission estimates constrained with MOPITT column and profile data
344 demonstrate significant positive trend in our study period, whereas the emission estimate
345 constrained with MOPITT lower tropospheric profile data shows a decreasing trend. Schneider et
346 al. (2015) showed that NO₂ over south Asia from SCIAMACHY is increasing in the period of
347 2003-2011. Using OMI NO₂ measurements, recent studies (e.g., Duncan et al. 2016) demonstrated
348 that NO₂ over India has a positive trend during 2005-2015. Observations from Cape Rama (CRI)
349 station (Figure 7d) demonstrate that CO concentration in 2010-2013 is significantly higher than
350 that in 2001-2002. For these reasons, we have more confidence in our results that indicate

351 increasing anthropogenic CO emissions from India and Southeast Asia in the past 15 years. The
352 trend based on the MOPITT lower-tropospheric data is incorrect because of model error in
353 convection in this dynamically varying region, and the negative bias drift in MOPITT lower
354 tropospheric retrievals (Deeter et al., 2014). The total anthropogenic CO emission (constrained
355 with MOPITT profile data) from India and Southeast Asia is 130.4 Tg in 2015, which is 34%
356 higher than that in 2001 (97.5 Tg). It should be noted that the inconsistency between our analysis
357 with Yin et al. (2015) suggests more studies are needed for robust conclusion about the variation
358 of anthropogenic CO emissions for this region.

359 Although our inverse analysis (constrained with MOPITT profile data) suggests similar
360 anthropogenic CO emissions from East China in 2008 and 2014, Figure 7c demonstrates that mean
361 CO concentrations over the outflow region of East China are 6 ppb higher in 2014 compared to
362 2008. Our previous study (Jiang et al. 2015c) indicated that anthropogenic emissions from India
363 and southeast Asia have an important influence on pollutant concentrations in the east China
364 outflow region. It is possible that the increase of CO concentration observed by WDCGG stations
365 in this region is caused by the significant increase of anthropogenic CO emission from India and
366 southeast Asia. In the most recent 5 years (2011-2015), our results (constrained with MOPITT
367 profile data) suggested a 20.5 Tg emission reduction from East China, and a 10.1 Tg emission
368 increase from India and Southeast Asia. Assuming a fixed emission growth rate, projected
369 anthropogenic CO emissions from India and Southeast Asia will overtake Chinese emissions in
370 2020, resulting in serious socioeconomic issues on both local and global scales.

371 **4.2.2. Regional analysis for biomass burning emissions**

372 Figure 8 and Table 2 show the regional variation of biomass burning emissions. There are
373 significant decreasing trends in three regions (i.e. boreal North America, boreal Asia, and South

374 America). Our results show high biomass burning emissions from boreal North America (mainly
375 Alaska and western Canada) in 2004 (Figure 8a), which have been reported by previous studies
376 (e.g. Pfister et al. 2005; Turquety et al. 2007), and also from boreal Asia during 2001-2003 (Figure
377 8b) due to significant fire activity in Siberia (e.g., Yurganov et al., 2005, Stroppiana et al., 2010).
378 For South America (Figure 8c), we found higher biomass burning emissions in the periods of 2004-
379 2007 and 2010, consistent with fire activity reported in previous studies (e.g. Hooghiemstra et al.
380 2012; Bloom et al. 2015).

381 Figure 8d shows the regional variation of biomass burning emissions from Africa. The fire
382 activities in Africa demonstrates obvious seasonality: peak in boreal winter for Northern
383 Hemispheric Africa, and in austral winter for Southern Hemispheric Africa. Similar to previous
384 studies (e.g. Chevallier et al. 2009; Tosca et al. 2015), there is no obvious emission trend in Africa
385 in the past 15 years. This is also consistent with the burned area trends described by Andela et al.
386 (2014) which show opposite directions for Northern Africa (decreasing) versus Southern Africa
387 (increasing) and would have cancelling effects in the trend for the continent as a whole.

388 Our results exhibit two strong biomass burning events in Indonesia, 2006 and 2015,
389 individually (Figure 8e). Previous studies (e.g. Logan et al. 2008; Zhang et al. 2011; Worden et al.
390 2013b, 2013c, Field et al., 2016) demonstrate the direct relationship between strong Indonesian
391 fires and El Niño. Recent studies (Huang et al. 2014; Inness et al. 2015) confirm low biomass
392 burning activities in Indonesia in the period of 2007-2012. CO emissions from the Indonesian fires
393 associated with the 2015 El Niño were 92 Tg (for October, 2015, as constrained with MOPITT
394 profile data), and were about three times higher than the October 2006 El Niño driven fire
395 emissions (32 Tg). Not including the 2015 El Niño driven fires, our analysis indicates a negative
396 trend of global biomass burning emissions in the past 15 years, as shown in Figure 11f.

397 **4.3. Changes in tropospheric CO during 2001-2015**

398 In this section, we evaluate our inversion results using independent long-term surface in-
399 situ measurements from WDCGG stations. Figure 9a shows the annual trend of surface CO
400 concentration for 2001 – 2015 from WDCGG sites, and from model simulations driven with a
401 priori emissions. Most WDCGG sites exhibit negative trends in the past 15 years, confirming the
402 decreasing trend of global tropospheric CO, which is consistent with satellite observations (e.g.
403 Warner et al. 2013; Worden et al. 2013). There are also stations with positive trends, for example,
404 Tae-ahn Peninsula (TAP, Korea), Ascension Island (ASC, equatorial Atlantic Ocean), Cape Rama
405 (CRI, India), Bukit Koto Tabang (BKT, Indonesia) and Cape Grim (CGO, Australia). Globally,
406 the a priori model simulation is in reasonable agreement with WDCGG measurements: both show
407 negative trends in middle/high latitude, and positive trends in some tropical regions. However,
408 there are noticeable discrepancies, for example, the surface observation from Yonagunijima (YON,
409 east China sea) shows a negative trend in our study period, suggesting decreasing trend from
410 Chinese CO emission, whereas the a priori simulation demonstrates significant positive trend.

411 Figure 9b-9d show the model simulations driven with a posteriori emissions. The a
412 posteriori emissions constrained with MOPITT lower tropospheric profile data (Figure 9d) results
413 in unrealistic large CO reduction, which could be caused by the negative bias drift of MOPITT
414 retrievals at lower troposphere (Deeter et al. 2014) and the influence from possible variability in
415 model convective transport. The a posteriori emissions constrained with MOPITT column and
416 profile data have similar comparisons. For example, both of them suggest a negative trend over
417 east China, consistent with observations from YON, and positive trend over northeast Asia,
418 consistent with observations from TAP.

419 In order to better compare the discrepancy between model simulation and surface

420 observations, Figure 9e-9g show the improvement due to a posteriori emissions, derived by
421 $\text{abs}(\text{Trend}_{\text{aposteriori}} - \text{Trend}_{\text{WDCGG}}) - \text{abs}(\text{Trend}_{\text{apriori}} - \text{Trend}_{\text{WDCGG}})$. Blue (red) means the a posteriori
422 emissions improves (degrades) the agreement with WDCGG measurements compared to the
423 simulated surface CO using a priori emissions, while white indicates no change from the prior. As
424 shown in Figure 9f, the CO emissions constrained with MOPITT profile data improved the model
425 simulation for most WDCGG sites in the Northern Hemisphere. The a posteriori emissions
426 constrained with MOPITT column data are somewhat worse, particularly over Europe, while CO
427 emissions constrained with MOPITT profile data over Europe give improved comparisons to
428 WDCGG surface CO measurements. Worden et al. (2010) demonstrated that the degrees of
429 freedom for signal (DFS) of MOPITT multi-spectral profile retrievals (TIR+NIR) is about 1.5-2.0
430 over land, which is reduced to about 1 DFS when converted to a total column. This reduction in
431 vertical information in MOPITT column data can affect the the reliability of inverse analysis
432 results (Jiang et al., 2015a). It should be noticed that the vertical correlation in model simulation
433 is not considered in our assimilation, which could be another possible reason for this discrepancy.

434 Figure 10a-10d show the long-term mean value of surface CO concentration for 2001 –
435 2015 from WDCGG sites, and model simulations driven with a priori and a posteriori emissions.
436 All simulations provide similar results for long-term mean value. Figure 10e-10g show the
437 improvement due to a posteriori emissions, derived by $\text{abs}(\text{CO}_{\text{aposteriori}} - \text{CO}_{\text{WDCGG}}) - \text{abs}(\text{CO}_{\text{apriori}}$
438 $- \text{CO}_{\text{WDCGG}})$. Figure 10f demonstrates that CO emissions constrained with MOPITT profile data
439 improved the model simulation in about half of the sites in the Northern Hemisphere, whereas the
440 a posteriori emissions constrained with MOPITT column data are somewhat worse (Figure 10e).
441 Evaluating modeled tracer concentrations using surface in-situ measurements is more challenging
442 than evaluating long-term trends. Important sources of uncertainty include the representation error

443 (e.g. Chang et al. 2015; Kharol et al. 2015) and vertical mixing of boundary layer (e.g. Castellanos
444 et al. 2011; Cuchiara et al. 2014).

445 Because our a posteriori simulation, particularly using emissions constrained with
446 MOPITT profile data, results in significant improvement in the long-term trend, and moderate
447 improvement in the mean value, we believe these a posteriori estimates provide a better description
448 for the long-term variation of global CO emissions. A remaining question is to explore how
449 changes in meterological conditions affect the long-term variation. By fixing CO emissions to
450 2001 levels, Figure 11a-11b show the long-term trend of modeled surface and column CO during
451 2001-2015, due only to changes in meterological conditions. At the surface level (Figure 11a), we
452 found changes in meterology result in a moderate positive trend in the Northern Hemisphere,
453 particularly, over northeast Asia, consistent with observation records from the TAP station; and
454 significant positive trend in tropics, consistent with observation record from ASC station. On the
455 other hand, the influence of meterological conditions on column CO (Figure 11b) is much weaker.
456 The discrepancy between surface and column CO suggests the possible contribution from variable
457 convective transport. It should be noted that our analysis for the contributions from meterological
458 conditions could be affected by the discrepancies among various versions of the meterological
459 fields (i.e. GEOS-4, GEOS-5 and GEOS-FP), and the lack of consistency in model physics of
460 GEOS-5 (e.g. the transition from GEOS 5.1.0 to GEOS 5.2.0 in late 2008).

461 Figure 11c-11h show the variation of global tropospheric CO due to changes in emissions.
462 Yin et al. (2015) indicated that the negative trend of tropospheric CO in the Northern Hemisphere
463 is driven by decreasing anthropogenic emissions from North America, Europe and China. Along
464 with reductions in anthropogenic emissions (Figure 11c, 11d), we found the decrease of biomass
465 burning emissions from boreal North America and boreal Asia (Figure 11e, 11f) to be an important

466 factor for this negative trend. In contrast to the emission reduction from North America, Europe
467 and China, we found increasing anthropogenic emissions from India and southeast Asia, which
468 result in a pronounced positive trend of tropospheric CO, while Yin et al. (2015) obtain a negative
469 trend for this region. This discrepancy requires further study and we will need to test the relative
470 importance of the primary differences in our methods, i.e., models and inversion approaches,
471 climatological OH (this study) vs. assimilated surface measurements of CH₄ and MCF to update
472 OH (Yin et al.) and the use of MOPITT profile vs. column CO retrievals (Yin et al., assimilate
473 only column CO).

474 **5. Summary**

475 The objective of this work is to investigate the dominant reasons for the observed variation
476 of global tropospheric CO over the past 15 years. We provide an update for this critical question
477 and also an updated CO emission estimates for model studies. In particular, we use surface
478 measurements of MCF to evaluate changes in the sinks of atmospheric CO, and constrain the
479 sources using MOPITT CO measurements to explain the observed decrease in CO concentrations.
480 Our two-step approach for estimating global CO emissions mitigates the effects of model errors
481 from transport and chemistry, as well as measurement bias error.

482 Using the same approach as Montzka et al. (2011), we assess the variation of tropospheric
483 OH (the primary CO sink) in the period of 2001-2015 using MCF measurements from WDCGG
484 stations. Our result demonstrates negligible variation of global tropospheric OH in the past 15
485 years, and consequently we suggest that the global sink of CO due to chemical loss through OH
486 has not likely changed during this time period. We therefore expect the decreasing trend of
487 tropospheric CO in North hemisphere (e.g. Warner et al. 2013; Worden et al. 2013; Gratz et al.
488 2015) to be driven by decreasing CO sources. Total anthropogenic CO emissions from the US

489 were 56.8 Tg in 2015, which are 35% lower than emissions in 2001 (87.7 Tg). Total anthropogenic
490 CO emissions from East China were 159.0 Tg in 2015, which are 7% lower than 2001 emissions
491 (170.4 Tg) and 23% lower than 2004 emissions (205.6 Tg). This pronounced decrease of emissions
492 from US and China is an indication of progress for fuel efficiency and emission control regulations.
493 Conversely, our results demonstrate that anthropogenic emissions from Europe decreased from
494 2001 to 2007 but are almost unchanged during 2008-2015. We also found a significant increase of
495 anthropogenic emissions for India and Southeast Asia. The total anthropogenic CO emission from
496 India and southeast Asia is 130.4 Tg in 2015, which is 34% higher than that in 2001 (97.5 Tg).
497 Assuming the same emission growth rate as 2011-2015, we expect that anthropogenic CO
498 emissions from India and Southeast Asia will be larger than Chinese emissions by 2020.

499 In a recent study, Yin et al. (2015) indicated that the decreasing tropospheric CO in the
500 Northern Hemisphere is caused by the decrease of anthropogenic emissions from North America,
501 Europe and China. We find that a decrease of biomass burning emissions from boreal North
502 America and boreal Asia is also an important contributor for the negative trend. Globally, our
503 analysis indicates a negative trend of biomass burning emissions in the past 15 years, except in
504 Indonesia due to the strong biomass burning event in 2015 associated with El Niño. Our results
505 demonstrate a significant decrease of biomass burning emissions from South America, which
506 could be associated with the reduction of deforestation in Brazil (Reddington et al. 2015), and the
507 predominant change from El Nino to La Nina in our study period (Andela et al. 2014). For Africa,
508 there is no obvious CO emission trend in the past 15 years, consistent with previous results
509 (Chevallier et al. 2009; Tosca et al. 2015; Andela et al., 2014). Our results are inconclusive in
510 characterizing the CO sources from oxidation of biogenic VOCs. More efforts are needed in the
511 future to better understand the mechanism for tropical CO emissions.

512 Our analysis highlights the importance of space-based instruments for monitoring changes
513 in global pollutant emissions. Our results demonstrate successful emission controls in US and
514 China over the past 15 years, and suggest that emission controls in Europe may need re-evaluation.
515 We also recommend more efforts in the future to better understand the regional and global effects
516 of increasing pollutant emissions from India and Southeast Asia.

517

518 **Acknowledgments.**

519 We thank the World Data Centre for Greenhouse Gases (WDCGG) for providing their CO
520 and MCF data. The National Center for Atmospheric Research (NCAR) is sponsored by the
521 National Science Foundation. The NCAR MOPITT project is supported by the National
522 Aeronautics and Space Administration (NASA) Earth Observing System (EOS) Program. The
523 MOPITT team also acknowledges support from the Canadian Space Agency (CSA), the Natural
524 Sciences and Engineering Research Council (NSERC) and Environment Canada, along with the
525 contributions of COMDEV (the prime contractor) and ABB BOMEM. MOPITT data sets used in
526 this study are publicly available at <http://reverb.echo.nasa.gov> and at
527 <https://eosweb.larc.nasa.gov/datapool>.

528

529 **Data availability**

530 The MOPITT data is available at <ftp://l5eil01.larc.nasa.gov/MOPITT/MOP02J.006>. The MCF and
531 CO measurements from WDCGG is available at <http://ds.data.jma.go.jp/gmd/wdcgg/>.

532

533 **References**

534 Andela, N., and van der Werf, G.: Recent trends in African fires driven by cropland expansion and

535 El Niño to La Niña transition, *Nature Climate Change* 4, 791–795, doi:10.1038/nclimate2313,
536 2014.

537 Arellano, A., Kasibhatla, P., Giglio, L., Werf, G., Randerson, J. and Collatz, G.: Time-dependent
538 inversion estimates of global biomass-burning CO emissions using Measurement of Pollution in
539 the Troposphere (MOPITT) measurements, *J Geophys Res Atmospheres* 1984 2012, 111(D9),
540 doi:10.1029/2005JD006613, 2006.

541 Bergamaschi, P., Frankenberg, C., Meirink, J., Krol, M., Dentener, F., Wagner, T., Platt, U.,
542 Kaplan, J., Körner, S., Heimann, M., Dlugokencky, E. and Goede, A.: Satellite chartography of
543 atmospheric methane from SCIAMACHY on board ENVISAT: 2. Evaluation based on inverse
544 model simulations, *J Geophys Res Atmospheres* 1984 2012, 112(D2),
545 doi:10.1029/2006JD007268, 2007.

546 Bergamaschi, P., Frankenberg, C., Meirink, J., Krol, M., Villani, M., Houweling, S., Dentener, F.,
547 Dlugokencky, E., Miller, J., Gatti, L., Engel, A. and Levin, I.: Inverse modeling of global and
548 regional CH₄ emissions using SCIAMACHY satellite retrievals, *J Geophys Res Atmospheres*
549 1984 2012, 114(D22), doi:10.1029/2009JD012287, 2009.

550 Bergamaschi, P., Houweling, S., Segers, A., Krol, M., Frankenberg, C., Scheepmaker, R.,
551 Dlugokencky, E., Wofsy, S., Kort, E., Sweeney, C., Schuck, T., Brenninkmeijer, C., Chen, H.,
552 Beck, V. and Gerbig, C.: Atmospheric CH₄ in the first decade of the 21st century: Inverse
553 modeling analysis using SCIAMACHY satellite retrievals and NOAA surface measurements, *J*
554 *Geophys Res Atmospheres*, 118(13), 7350–7369, doi:10.1002/jgrd.50480, 2013.

555 Bloom, A., Worden, J., Jiang, Z., Worden, H., Kurosu, T., Frankenberg, C. and Schimel, D.:
556 Remote-sensing constraints on South America fire traits by Bayesian fusion of atmospheric and
557 surface data, *Geophys Res Lett*, 42(4), 1268–1274, doi:10.1002/2014GL062584, 2015.

558 Bousquet, P., Hauglustaine, D. A., Peylin, P., Carouge, C., and Ciais, P.: Two decades of OH
559 variability as inferred by an inversion of atmospheric transport and chemistry of methyl
560 chloroform, *Atmos. Chem. Phys.*, 5, 2635-2656, doi:10.5194/acp-5-2635-2005, 2005.

561 Bouscerez, N., Henze, D., Perkins, A., Bowman, K., Lee, M., Liu, J., Deng, F. and Jones, D.:
562 Improved analysis-error covariance matrix for high-dimensional variational inversions:
563 application to source estimation using a 3D atmospheric transport model, *Q J Roy Meteor Soc*,
564 141(690), 1906–1921, doi:10.1002/qj.2495, 2015.

565 Bruhwiler, L., Dlugokencky, E., Masarie, K., Ishizawa, M., Andrews, A., Miller, J., Sweeney, C.,
566 Tans, P., and Worthy, D.: CarbonTracker-CH₄: an assimilation system for estimating emissions
567 of atmospheric methane, *Atmos. Chem. Phys.*, 14, 8269-8293, doi:10.5194/acp-14-8269-2014,
568 2014.

569 Castellanos, P., Marufu, L., Doddridge, B., Taubman, B., Schwab, J., Hains, J., Ehrman, S. and
570 Dickerson, R.: Ozone, oxides of nitrogen, and carbon monoxide during pollution events over the
571 eastern United States: An evaluation of emissions and vertical mixing, *J Geophys Res
572 Atmospheres* 1984 2012, 116(D16), doi:10.1029/2010JD014540, 2011.

573 Chang, K.-L., Guillas, S., and Fioletov, V. E.: Spatial mapping of ground-based observations of
574 total ozone, *Atmos. Meas. Tech.*, 8, 4487-4505, doi:10.5194/amt-8-4487-2015, 2015.

575 Chevallier, F., Fortems, A., Bousquet, P., Pison, I., Szopa, S., Devaux, M. and Hauglustaine, D.:
576 African CO emissions between years 2000 and 2006 as estimated from MOPITT observations,
577 *Biogeosciences*, 6(1), 103–111, doi:10.5194/bg-6-103-2009, 2009.

578 Cuchiara, G. C., Li, X., Carvalho, J. and Rappenglück, B.: Intercomparison of planetary boundary
579 layer parameterization and its impacts on surface ozone concentration in the WRF/Chem model
580 for a case study in Houston/Texas, *Atmos Environ.*, 96, 175–185,

581 doi:10.1016/j.atmosenv.2014.07.013, 2014.

582 Deeter, M., Worden, H., Gille, J., Edwards, D., Mao, D. and Drummond, J.: MOPITT multispectral
583 CO retrievals: Origins and effects of geophysical radiance errors, *J Geophys Res Atmospheres*
584 1984 2012, 116(D15), doi:10.1029/2011JD015703, 2011.

585 Deeter, M. N., Martínez-Alonso, S., Edwards, D. P., Emmons, L. K., Gille, J. C., Worden, H. M.,
586 Sweeney, C., Pittman, J. V., Daube, B. C., and Wofsy, S. C.: The MOPITT Version 6 product:
587 algorithm enhancements and validation, *Atmos. Meas. Tech.*, 7, 3623-3632, doi:10.5194/amt-7-
588 3623-2014, 2014.

589 Deng, F., Jones, D. B. A., Henze, D. K., Bouscerez, N., Bowman, K. W., Fisher, J. B., Nassar, R.,
590 O'Dell, C., Wunch, D., Wennberg, P. O., Kort, E. A., Wofsy, S. C., Blumenstock, T., Deutscher,
591 N. M., Griffith, D. W. T., Hase, F., Heikkinen, P., Sherlock, V., Strong, K., Sussmann, R., and
592 Warneke, T.: Inferring regional sources and sinks of atmospheric CO₂ from GOSAT XCO₂ data,
593 *Atmos. Chem. Phys.*, 14, 3703-3727, doi:10.5194/acp-14-3703-2014, 2014.

594 Duncan, B., Lamsal, L., Thompson, A., Yoshida, Y., Lu, Z., Streets, D., Hurwitz, M. and
595 Pickering, K.: A space-based, high-resolution view of notable changes in urban NO_x pollution
596 around the world (2005–2014), *J Geophys Res Atmospheres*, 121(2), 976–996,
597 doi:10.1002/2015JD024121, 2016.

598 Evans, M. J., and Jacob, D. J.: Impact of new laboratory studies of N₂O₅ hydrolysis on global
599 model budgets of tropospheric nitrogen oxides, ozone, and OH, *Geophys. Res. Lett.*, 32, L09813,
600 doi:10.1029/2005GL022469, 2005.

601 Field, R. et al., 2015 Indonesian fire activity and smoke pollution show persistent non-linear
602 sensitivity to El Niño-induced drought, *PNAS*, 2016, 9204–9209, doi: 10.1073/pnas.1524888113

603 Fortems-Cheiney, A., Chevallier, F., Pison, I., Bousquet, P., Szopa, S., Deeter, M. and Clerbaux,

604 C.: Ten years of CO emissions as seen from Measurements of Pollution in the Troposphere
605 (MOPITT), *J Geophys Res Atmospheres* 1984 2012, 116(D5), doi:10.1029/2010JD014416,
606 2011.

607 Fortems-Cheiney, A., Chevallier, F., Pison, I., Bousquet, P., Saunois, M., Szopa, S., Cressot, C.,
608 Kurosu, T. P., Chance, K., and Fried, A.: The formaldehyde budget as seen by a global-scale
609 multi-constraint and multi-species inversion system, *Atmos. Chem. Phys.*, 12, 6699-6721,
610 doi:10.5194/acp-12-6699-2012, 2012.

611 Gonzi, S., Feng, L. and Palmer, P.: Seasonal cycle of emissions of CO inferred from MOPITT
612 profiles of CO: Sensitivity to pyroconvection and profile retrieval assumptions, *Geophys Res*
613 *Lett*, 38(8), n/a–n/a, doi:10.1029/2011GL046789, 2011.

614 Gratz, L. E., Jaffe, D. A. and Hee, J. R.: Causes of increasing ozone and decreasing carbon
615 monoxide in springtime at the Mt. Bachelor Observatory from 2004 to 2013, *Atmos Environ*,
616 109, 323–330, doi:10.1016/j.atmosenv.2014.05.076, 2015.

617 Guenther, A., Karl, T., Harley, P., Wiedinmyer, C., Palmer, P.I., and Geron, C.: Estimates of global
618 terrestrial isoprene emissions using MEGAN (Model of Emissions of Gases and Aerosols from
619 Nature), *Atmos. Chem. Phys.*, 6, 3181-3210, doi:10.5194/acp-6-3181-2006, 2006.

620 Heald, C., Jacob, D., Jones, D., Palmer, P., Logan, J., Streets, D., Sachse, G., Gille, J., Hoffman,
621 R. and Nehrkom, T.: Comparative inverse analysis of satellite (MOPITT) and aircraft (TRACE-
622 P) observations to estimate Asian sources of carbon monoxide, *J Geophys Res Atmospheres* 1984
623 2012, 109, D23306, doi:10.1029/2004JD005185, 2004.

624 Henschel, S., Tertre, A., Atkinson, R., Querol, X., Pandolfi, M., Zeka, A., Haluza, D., Analitis, A.,
625 Katsouyanni, K., Bouland, C., Pascal, M., Medina, S. and Goodman, P.: Trends of nitrogen
626 oxides in ambient air in nine European cities between 1999 and 2010, *Atmos Environ*, 117, 234–

627 241, doi:10.1016/j.atmosenv.2015.07.013, 2015.

628 Henze, D. K., Hakami, A., and Seinfeld, J. H.: Development of the adjoint of GEOS-Chem, Atmos.

629 Chem. Phys., 7, 2413-2433, doi:10.5194/acp-7-2413-2007, 2007.

630 Hidy, G., Blanchard, C., Baumann, K., Edgerton, E., Tanenbaum, S., Shaw, S., Knipping, E.,

631 Tombach, I., Jansen, J. and Walters, J.: Chemical climatology of the southeastern United States,

632 1999–2013, Atmos Chem Phys, 14(21), 11893–11914, doi:10.5194/acp-14-11893-2014, 2014.

633 Hilboll, A., Richter, A., and Burrows, J. P.: Long-term changes of tropospheric NO₂ over

634 megacities derived from multiple satellite instruments, Atmos. Chem. Phys., 13, 4145-4169,

635 doi:10.5194/acp-13-4145-2013, 2013.

636 Hooghiemstra, P., Krol, M., Leeuwen, T., Werf, G., Novelli, P., Deeter, M., Aben, I. and

637 Röckmann, T.: Interannual variability of carbon monoxide emission estimates over South

638 America from 2006 to 2010, J Geophys Res Atmospheres 1984 2012, 117(D15), n/a–n/a,

639 doi:10.1029/2012JD017758, 2012.

640 Houweling, S., Krol, M., Bergamaschi, P., Frankenberg, C., Dlugokencky, E. J., Morino, I.,

641 Notholt, J., Sherlock, V., Wunch, D., Beck, V., Gerbig, C., Chen, H., Kort, E. A., Röckmann,

642 T., and Aben, I.: A multi-year methane inversion using SCIAMACHY, accounting for

643 systematic errors using TCCON measurements, Atmos. Chem. Phys., 14, 3991-4012,

644 doi:10.5194/acp-14-3991-2014, 2014.

645 Huang, L., Fu, R., and Jiang, J. H.: Impacts of fire emissions and transport pathways on the

646 interannual variation of CO in the tropical upper troposphere, Atmos. Chem. Phys., 14, 4087-

647 4099, doi:10.5194/acp-14-4087-2014, 2014.

648 Inness, A., Benedetti, A., Flemming, J., Huijnen, V., Kaiser, J. W., Parrington, M., and Remy, S.:

649 The ENSO signal in atmospheric composition fields: emission-driven versus dynamically

650 induced changes, *Atmos. Chem. Phys.*, 15, 9083–9097, doi:10.5194/acp-15-9083-2015, 2015.

651 Jiang, Z., Jones, D., Kopacz, M., Liu, J., Henze, D. and Heald, C.: Quantifying the impact of model
652 errors on top-down estimates of carbon monoxide emissions using satellite observations, *J
653 Geophys Res Atmospheres* 1984 2012, 116(D15), doi:10.1029/2010JD015282, 2011.

654 Jiang, Z., Jones, D., Worden, H., Deeter, M., Henze, D., Worden, J., Bowman, K., Brenninkmeijer,
655 C. and Schuck, T.: Impact of model errors in convective transport on CO source estimates
656 inferred from MOPITT CO retrievals, *J Geophys Res Atmospheres*, 118(4), 2073–2083,
657 doi:10.1002/jgrd.50216, 2013.

658 Jiang, Z., Jones, D., Worden, H. and Henze, D.: Sensitivity of top-down CO source estimates to
659 the modeled vertical structure in atmospheric CO, *Atmos Chem Phys*, 15(3), 1521–1537,
660 doi:10.5194/acp-15-1521-2015, 2015a.

661 Jiang, Z., Jones, D., Worden, J., Worden, H., Henze, D. and Wang, Y.: Regional data assimilation
662 of multi-spectral MOPITT observations of CO over North America, *Atmos Chem Phys*, 15(12),
663 6801–6814, doi:10.5194/acp-15-6801-2015, 2015b.

664 Jiang, Z., Worden, J. R., Jones, D. B. A., Lin, J.-T., Verstraeten, W. W., and Henze, D. K.:
665 Constraints on Asian ozone using Aura TES, OMI and Terra MOPITT, *Atmos. Chem. Phys.*, 15,
666 99–112, doi:10.5194/acp-15-99-2015, 2015c.

667 Jones, D., Bowman, K., Logan, J., Heald, C., Liu, J., Luo, M., Worden, J. and Drummond, J.: The
668 zonal structure of tropical O₃ and CO as observed by the Tropospheric Emission Spectrometer
669 in November 2004 – Part 1: Inverse modeling of CO emissions, *Atmos Chem Phys*, 9(11), 3547–
670 3562, doi:10.5194/acp-9-3547-2009, 2009.

671 Kharol, S. K., Martin, R. V., Philip, S., Boys, B., Lamsal, L. N., Jerrett, M., Brauer, M., Crouse,
672 D. L., McLinden, C. and Burnett, R. T.: Assessment of the magnitude and recent trends in

673 satellite-derived ground-level nitrogen dioxide over North America, *Atmos Environ*, 118, 236–
674 245, doi:10.1016/j.atmosenv.2015.08.011, 2015.

675 Kopacz, M., Jacob, D., Henze, D., Heald, C., Streets, D. and Zhang, Q.: Comparison of adjoint
676 and analytical Bayesian inversion methods for constraining Asian sources of carbon monoxide
677 using satellite (MOPITT) measurements of CO columns, *J Geophys Res Atmospheres* 1984
678 2012, 114(D4), doi:10.1029/2007JD009264, 2009.

679 Kopacz, M., Jacob, D., Fisher, J., Logan, J., Zhang, L., Megretskaya, I., Yantosca, R., Singh, K.,
680 Henze, D., Burrows, J., Buchwitz, M., Khlystova, I., McMillan, W., Gille, J., Edwards, D.,
681 Eldering, A., Thouret, V. and Nedelec, P.: Global estimates of CO sources with high resolution
682 by adjoint inversion of multiple satellite datasets (MOPITT, AIRS, SCIAMACHY, TES), *Atmos*
683 *Chem Phys*, 10(3), 855–876, doi:10.5194/acp-10-855-2010, 2010.

684 Krol, M., vanLeeuwen, P. J., and Lelieveld, J.: Global OH trend inferred from methylchloroform
685 measurements, *J. Geophys. Res.*, 103(D9), 10697–10711, doi:[10.1029/98JD00459](https://doi.org/10.1029/98JD00459), 1998.

686 Kuhns, H., Green, M. and Etyemezian, V.: Big Bend Regional Aerosol and Visibility
687 Observational (BRAVO) Study Emissions Inventory, Report prepared for BRAVO Steering
688 Committee, Desert Research Institute, Las Vegas, Nevada, 2003.

689 Kumar, A., Wu, S., Weise, M. F., Honrath, R., Owen, R. C., Helmig, D., Kramer, L., Val Martin,
690 M., and Li, Q.: Free-troposphere ozone and carbon monoxide over the North Atlantic for 2001–
691 2011, *Atmos. Chem. Phys.*, 13, 12537–12547, doi:10.5194/acp-13-12537-2013, 2013.

692 Lelieveld, J., Dentener, F., Peters, W. and Krol, M.: On the role of hydroxyl radicals in the self-
693 cleansing capacity of the troposphere, *Atmos Chem Phys*, 4(9/10), 2337–2344, doi:10.5194/acp-
694 4-2337-2004, 2004.

695 Liu, F., Zhang, Q., Tong, D., Zheng, B., Li, M., Huo, H., and He, K. B.: High-resolution inventory

696 of technologies, activities, and emissions of coal-fired power plants in China from 1990 to 2010,
697 *Atmos. Chem. Phys.*, 15, 13299-13317, doi:10.5194/acp-15-13299-2015, 2015.

698 Logan, J., Megretskaya, I., Nassar, R., Murray, L., Zhang, L., Bowman, K., Worden, H. and Luo,
699 M.: Effects of the 2006 El Niño on tropospheric composition as revealed by data from the
700 Tropospheric Emission Spectrometer (TES), *Geophys. Res. Lett.*, 35(3),
701 doi:10.1029/2007GL031698, 2008.

702 Meirink, J., Bergamaschi, P., Frankenberg, C., Amelio, M. d', Dlugokencky, E., Gatti, L.,
703 Houweling, S., Miller, J., Röckmann, T., Villani, M. and Krol, M.: Four-dimensional variational
704 data assimilation for inverse modeling of atmospheric methane emissions: Analysis of
705 SCIAMACHY observations, *J. Geophys. Res. Atmospheres* 1984–2012, 113(D17),
706 doi:10.1029/2007JD009740, 2008.

707 Miyazaki, K., Eskes, H. and Sudo, K.: A tropospheric chemistry reanalysis for the years 2005–
708 2012 based on an assimilation of OMI, MLS, TES, and MOPITT satellite data, *Atmos. Chem.*
709 *Phys.*, 15(14), 8315–8348, doi:10.5194/acp-15-8315-2015, 2015.

710 Montzka, S. A., Krol, M., Dlugokencky, E., Hall, B., Jöckel, P., Lelieveld, J.: Small Interannual
711 Variability of Global Atmospheric Hydroxyl, *Science*, 331(6013), 67–69,
712 10.1126/science.1197640, 2011.

713 Ohara, T., Akimoto, H., Kurokawa, J., Horii, N., Yamaji, K., Yan, X. and Hayasaka, T.: An Asian
714 emission inventory of anthropogenic emission sources for the period 1980–2020, *Atmos. Chem.*
715 *Phys.*, 7(16), 4419–4444, doi:10.5194/acp-7-4419-2007, 2007.

716 Pfister, G., Hess, P., Emmons, L., Lamarque, J. -F., Wiedinmyer, C., Edwards, D., Pétron, G.,
717 Gille, J. and Sachse, G.: Quantifying CO emissions from the 2004 Alaskan wildfires using
718 MOPITT CO data, *Geophys. Res. Lett.*, 32(11), doi:10.1029/2005GL022995, 2005.

719 Prinn, R., Huang, J., Weiss, R., Cunnold, D., Fraser, P., Simmonds, P., McCulloch, A., Harth, C.,
720 Reimann, S., Salameh, P., O'Doherty, S., Wang, R., Porter, L., Miller, B. and Krummel, P.:
721 Evidence for variability of atmospheric hydroxyl radicals over the past quarter century, *Geophys*
722 *Res Lett*, 32(7), n/a–n/a, doi:10.1029/2004GL022228, 2005.

723 Reddington, C., Butt, E., Ridley, D., Artaxo, P., Morgan, W., Coe, H. and Spracklen, D.: Air
724 quality and human health improvements from reductions in deforestation-related fire in Brazil,
725 *Nat Geosci*, 8(10), 768–771, doi:10.1038/ngeo2535, 2015.

726 Schneider, P., Lahoz, W. A., and van der A, R.: Recent satellite-based trends of tropospheric
727 nitrogen dioxide over large urban agglomerations worldwide, *Atmos. Chem. Phys.*, 15, 1205–
728 1220, doi:10.5194/acp-15-1205-2015, 2015.

729 Spivakovsky, C. M., Logan, J. A., Montzka, S. A., Balkanski, Y. J., Foreman-Fowler, M., Jones,
730 D. B. A., Horowitz, L. W., Fusco, A. C., Brenninkmeijer, C. A. M., Prather, M. J., Wofsy, S. C.
731 and McElroy, M. B.: Three-dimensional climatological distribution of tropospheric OH Update
732 and evaluation, *J. Geophys. Res.*, 105(D7), 8931–8980, doi:10.1029/1999JD901006, 2000.

733 Streets, D., Zhang, Q., Wang, L., He, K., Hao, J., Wu, Y., Tang, Y. and Carmichael, G.: Revisiting
734 China's CO emissions after the Transport and Chemical Evolution over the Pacific (TRACE-P)
735 mission: Synthesis of inventories, atmospheric modeling, and observations, *J Geophys Res*
736 *Atmospheres* 1984 2012, 111(D14), doi:10.1029/2006JD007118, 2006.

737 Strode, S., Worden, H., Damon, M., Douglass, A., Duncan, B., Emmons, L., Lamarque, J.-F.,
738 Manyin, M., Oman, L., Rodriguez, J., Strahan, S. and Tilmes, S.: Interpreting space-based trends
739 in carbon monoxide with multiple models, *Atmos. Chem. Phys.*, 16(11), 7285–7294,
740 doi:10.5194/acp-16-7285-2016, 2016.

741 Stroppiana, D., Brivio, P. A., Grégoire, J.-M., Liousse, C., Guillaume, B., Granier, C., Mieville,

742 A., Chin, M., and Pétron, G.: Comparison of global inventories of CO emissions from biomass
743 burning derived from remotely sensed data, *Atmos. Chem. Phys.*, 10, 12173-12189,
744 doi:10.5194/acp-10-12173-2010, 2010.

745 Tohjima, Y., Kubo, M., Minejima, C., Mukai, H., Tanimoto, H., Ganshin, A., Maksyutov, S.,
746 Katsumata, K., Machida, T., and Kita, K.: Temporal changes in the emissions of CH₄ and CO
747 from China estimated from CH₄ / CO₂ and CO / CO₂ correlations observed at Hateruma Island,
748 *Atmos. Chem. Phys.*, 14, 1663-1677, doi:10.5194/acp-14-1663-2014, 2014.

749 Tosca, M., Diner, D., Garay, M. and Kalashnikova, O.: Human-caused fires limit convection in
750 tropical Africa: First temporal observations and attribution, *Geophys Res Lett*, 42(15), 6492–
751 6501, doi:10.1002/2015GL065063, 2015.

752 Turquety, S., Logan, J., Jacob, D., Hudman, R., Leung, F., Heald, C., Yantosca, R., Wu, S.,
753 Emmons, L., Edwards, D. and Sachse, G.: Inventory of boreal fire emissions for North America
754 in 2004: Importance of peat burning and pyroconvective injection, *J Geophys Res Atmospheres*
755 1984 2012, 112(D12), doi:10.1029/2006JD007281, 2007.

756 Turner, A. J., Jacob, D. J., Wecht, K. J., Maasakkers, J. D., Lundgren, E., Andrews, A. E., Biraud,
757 S. C., Boesch, H., Bowman, K. W., Deutscher, N. M., Dubey, M. K., Griffith, D. W. T., Hase,
758 F., Kuze, A., Notholt, J., Ohyama, H., Parker, R., Payne, V. H., Sussmann, R., Sweeney, C.,
759 Velazco, V. A., Warneke, T., Wennberg, P. O., and Wunch, D.: Estimating global and North
760 American methane emissions with high spatial resolution using GOSAT satellite data, *Atmos.*
761 *Chem. Phys.*, 15, 7049-7069, doi:10.5194/acp-15-7049-2015, 2015.

762 van der Werf, G. R., Randerson, J. T., Giglio, L., Collatz, G. J., Kasibhatla, P. S., and Arellano Jr.,
763 A. F.: Interannual variability in global biomass burning emissions from 1997 to 2004, *Atmos.*
764 *Chem. Phys.*, 6, 3423-3441, doi:10.5194/acp-6-3423-2006, 2006.

765 van der Werf, G. R., Randerson, J. T., Giglio, L., Collatz, G. J., Mu, M., Kasibhatla, P. S.,
766 Morton, D. C., DeFries, R. S., Jin, Y., and van Leeuwen, T. T.: Global fire emissions and the
767 contribution of deforestation, savanna, forest, agricultural, and peat fires (1997–2009), *Atmos.*
768 *Chem. Phys.*, 10, 11707–11735, doi:10.5194/acp-10-11707-2010, 2010.

769 van Leeuwen, T. T. and van der Werf, G. R.: Spatial and temporal variability in the ratio of trace
770 gases emitted from biomass burning, *Atmos. Chem. Phys.*, 11, 3611-3629, doi:10.5194/acp-11-
771 3611-2011, 2011.

772 Vestreng, V. and Klein, H.: Emission data reported to UNECE/EMEP. Quality assurance and trend
773 analysis and Presentation of WebDab, Norwegian Meteorological Institute, Oslo, Norway, MSC-
774 W Status Report, 2002.

775 Warner, J., Carminati, F., Wei, Z., Lahoz, W., and Attié, J.-L.: Tropospheric carbon monoxide
776 variability from AIRS under clear and cloudy conditions, *Atmos. Chem. Phys.*, 13, 12469-12479,
777 doi:10.5194/acp-13-12469-2013, 2013.

778 Worden, H., Deeter, M., Edwards, D., Gille, J., Drummond, J. and Nédélec, P.: Observations of
779 near-surface carbon monoxide from space using MOPITT multispectral retrievals, *J Geophys*
780 *Res Atmospheres* 1984 2012, 115(D18), doi:10.1029/2010JD014242, 2010.

781 Worden, H. M., Deeter, M. N., Frankenberg, C., George, M., Nichitiu, F., Worden, J., Aben, I.,
782 Bowman, K. W., Clerbaux, C., Coheur, P. F., de Laat, A. T. J., Detweiler, R., Drummond, J. R.,
783 Edwards, D. P., Gille, J. C., Hurtmans, D., Luo, M., Martínez-Alonso, S., Massie, S., Pfister, G.,
784 and Warner, J. X.: Decadal record of satellite carbon monoxide observations, *Atmos. Chem.*
785 *Phys.*, 13, 837-850, doi:10.5194/acp-13-837-2013, 2013.

786 Worden, J., Wecht, K., Frankenberg, C., Alvarado, M., Bowman, K., Kort, E., Kulawik, S., Lee,
787 M., Payne, V., and Worden, H.: CH₄ and CO distributions over tropical fires during October

788 2006 as observed by the Aura TES satellite instrument and modeled by GEOS-Chem, Atmos.
789 Chem. Phys., 13, 3679-3692, doi:10.5194/acp-13-3679-2013, 2013b.

790 Worden, J., Jiang, Z., Jones, D., Alvarado, M., Bowman, K., Frankenberg, C., Kort, E., Kulawik,
791 S., Lee, M., Liu, J., Payne, V., Wecht, K. and Worden, H.: El Niño, the 2006 Indonesian peat
792 fires, and the distribution of atmospheric methane, Geophys Res Lett, 40(18), 4938–4943,
793 doi:10.1002/grl.50937, 2013c.

794 Xia, Y., Zhao, Y. and Nielsen, C.: Benefits of China's efforts in gaseous pollutant control indicated
795 by the bottom-up emissions and satellite observations 2000–2014, Atmos Environ, 136, 43–53,
796 doi:10.1016/j.atmosenv.2016.04.013, 2016.

797 Yin, Y., Chevallier, F., Ciais, P., Broquet, G., Fortems-Cheiney, A., Pison, I. and Saunois, M.:
798 Decadal trends in global CO emissions as seen by MOPITT, Atmos Chem Phys, 15(23), 13433–
799 13451, doi:10.5194/acp-15-13433-2015, 2015.

800 Yurganov, L. N., Duchatelet, P., Dzhola, A. V., Edwards, D. P., Hase, F., Kramer, I., Mahieu, E.,
801 Mellqvist, J., Notholt, J., Novelli, P. C., Rockmann, A., Scheel, H. E., Schneider, M., Schulz,
802 A., Strandberg, A., Sussmann, R., Tanimoto, H., Velazco, V., Drummond, J. R., and Gille, J. C.:
803 Increased Northern Hemispheric carbon monoxide burden in the troposphere in 2002 and 2003
804 detected from the ground and from space, Atmos. Chem. Phys., 5, 563-573, doi:10.5194/acp-5-
805 563-2005, 2005.

806 Zhang, Q., Streets, D., Carmichael, G., He, K., Huo, H., Kannari, A., Klimont, Z., Park, I., Reddy,
807 S., Fu, J., Chen, D., Duan, L., Lei, Y., Wang, L. and Yao, Z.: Asian emissions in 2006 for the
808 NASA INTEX-B mission, Atmos Chem Phys, 9(14), 5131–5153, doi:10.5194/acp-9-5131-2009,
809 2009.

810 Zhang, L., Li, Q. B., Jin, J., Liu, H., Livesey, N., Jiang, J. H., Mao, Y., Chen, D., Luo, M., and

811 Chen, Y.: Impacts of 2006 Indonesian fires and dynamics on tropical upper tropospheric carbon
812 monoxide and ozone, *Atmos. Chem. Phys.*, 11, 10929-10946, doi:10.5194/acp-11-10929-2011,
813 2011.

814 Zhao, Y., Nielsen, C., McElroy, M., Zhang, L. and Zhang, J.: CO emissions in China: Uncertainties
815 and implications of improved energy efficiency and emission control, *Atmos Environ*, 49, 103–
816 113, doi:10.1016/j.atmosenv.2011.12.015, 2012.

817

818 **Tables and Figures**

819 **Table 1.** Annual total anthropogenic CO emission in different regions, from 2001 to 2015,
820 constrained with MOPITT column, profile and lower tropospheric data. The region definition is
821 shown in Figure 2e.

822 **Table 2.** Annual total biomass burning CO emission in different regions, from 2001 to 2015,
823 constrained with MOPITT column, profile and lower tropospheric data. The region definition is
824 shown in Figure 2f.

825 **Figure 1.** Difference between MOPITT CO retrievals and HIPPO aircraft measurements. The
826 aircraft measurements are smoothed with MOPITT averaging kernels. The black solid line shows
827 the 4-order polynomial curve fitting, which is used to correct MOPITT data in this work.

828 **Figure 2.** (a-d) Mean a priori CO emissions from combustion sources and the oxidation of biogenic
829 VOCs and CH₄ from 2001 to 2015. The unit is 10¹² molec/cm²/sec. (e-f) Region definitions for (e)
830 anthropogenic and (f) biomass burning sources.

831 **Figure 3.** Schematic diagram for methodology of the assimilation system. Sequential Kalman
832 Filter was run from March 1 2000 to December 31 2015 to produce the optimized initial conditions
833 (monthly) and boundary conditions (hourly). Monthly 4-DVAR inversions were performed with
834 the optimized initial conditions. Only MOPITT data over land (white grids) were assimilated in
835 the 4-DVAR inversions, while the CO abundances over ocean (red grids) were defined as
836 boundaries and rewritten using the optimized hourly CO fields from Kalman Filter. The Kalman
837 filter run is completely independent of the 4-DVAR inversions. There is no feedback of the 4-
838 DVAR inversion results to the boundary conditions.

839 **Figure 4.** (a) Locations of WDCGG sites with MCF measurements. (b) Global mean MCF
840 concentration. (c) Exponential loss rate of MCF, derived from 12-month apart of monthly means
841 [e.g., ln(MCF_{Jan2007}/MCF_{Jan2006})]. The black solid line shows the 12-month mean value.

842

848 **Figure 5.** CO emission trends for 2001 – 2015, constrained with MOPITT column, profile and
849 lower tropospheric profile data. The months dominated by biomass burning emissions are excluded
850 from the trend calculation for anthropogenic and biogenic VOC emissions.

851
852 **Figure 6.** 12-month mean value of anthropogenic CO emissions (with unit Tg/month) for 2001 –
853 2015: a priori emission (green) and a posteriori emissions constrained with MOPITT column data
854 (black), MOPITT profile data (blue) and MOPITT lower tropospheric profile data (red). The green
855 dash line shows the monthly a priori anthropogenic CO emissions. The region definition is shown
856 in Figure 2e.

857
858 **Figure 7.** Monthly mean CO concentrations (green) and 12-month mean value (black) from
859 WDCGG stations for 2001 – 2015. (a) 15-station average in United States (b) 20-station average
860 in Europe (c) 2-station (YON and JMA) average in east China outflow (4) Cape Rama (CRI) in
861 India.

862
863 **Figure 8.** Monthly biomass burning CO emissions (with unit Tg/month) for 2001 – 2015: a priori
864 emission (green) and a posteriori emissions constrained with MOPITT column data (black),
865 MOPITT profile data (blue) and MOPITT lower tropospheric profile data (red). The region
866 definition is shown in Figure 2f.

867
868 **Figure 9.** Panels (a-d): long-term trend (annual) of surface CO concentration for 2001 – 2015 from
869 WDCGG sites, and model simulations driven with a priori and a posteriori emissions. Panels (e-
870 g): effect of a posteriori emissions, derived by $\text{abs}(\text{Trend}_{\text{aposteriori}} - \text{Trend}_{\text{WDCGG}}) - \text{abs}(\text{Trend}_{\text{apriori}} -$
871 $\text{Trend}_{\text{WDCGG}})$; blue (red) means the a posteriori emissions improves (degrades) the agreement with
872 WDCGG measurements compared to the a priori emissions, while white indicates no change from
873 the priori. Only stations with more than 10 year observations (the time range between the first and
874 last observations) during 2001-2015 are included.

875
876 **Figure 10.** Panels (a-d): long-term mean value of surface CO concentration for 2001 – 2015 from
877 WDCGG sites, and model simulations driven with a priori and a posteriori emissions. Panels (e-
878 g): effect of a posteriori emissions, derived by $\text{abs}(\text{CO}_{\text{aposteriori}} - \text{CO}_{\text{WDCGG}}) - \text{abs}(\text{CO}_{\text{apriori}} -$
879 $\text{CO}_{\text{WDCGG}})$; blue (red) means the a posteriori emissions improves (degrades) the agreement with
880 WDCGG measurements compared to the a priori emissions, while white indicates no change from
881 the priori. Only stations with more than 10 year observations (the time range between the first and
882 last observations) during 2001-2015 are included.

883
884 **Figure 11.** Long-term trend (annual) of modeled surface and column CO for 2001 – 2015 with (a-
885 b) all emission sources are fixed at 2001 level. (c-d) variable anthropogenic emissions; (e-f)
886 variable biomass burning emissions; (g-h) variable biogenic VOCs emissions; The variable
887 emissions are constrained with MOPITT profile data.

Years	MOPITT Column (Tg/year)					MOPITT Profile (Tg/year)					MOPITT Lower Profile (Tg/year)				
	United States	Europe	E China	India/SE Asia	Gobal Total	United States	Europe	E China	India/SE Asia	Gobal Total	United States	Europe	E China	India/SE Asia	Gobal Total
2001	87.8	71.6	165.7	102.2	526.5	87.7	77.3	170.4	97.5	522.9	112.9	92.0	215.7	136.1	677.5
2002	84.1	65.9	171.3	93.3	508.9	82.3	77.1	176.1	81.1	504.2	110.1	89.8	221.9	119.8	658.2
2003	80.8	65.3	178.8	95.4	516.2	80.4	74.5	189.2	88.5	523.2	103.6	87.0	218.1	121.9	645.1
2004	77.4	65.5	178.5	105.0	524.5	91.1	83.8	205.6	113.8	596.6	103.0	89.5	222.8	124.6	652.7
2005	72.7	64.6	178.6	104.3	518.0	82.6	79.4	200.6	116.8	581.5	92.7	84.5	215.3	126.2	630.6
2006	74.6	61.5	172.7	98.1	500.7	85.6	74.5	197.7	111.0	567.6	93.9	78.9	205.1	118.1	603.1
2007	73.7	56.5	177.1	105.8	511.4	84.0	67.9	200.9	113.2	568.2	90.9	71.8	208.1	119.4	599.6
2008	67.1	55.5	150.2	102.1	473.5	77.2	65.4	175.4	110.2	530.8	83.9	69.6	175.0	111.1	548.4
2009	66.0	54.8	162.0	105.7	486.0	74.5	65.1	185.9	118.3	544.1	78.0	67.0	184.5	115.1	547.4
2010	59.2	54.5	159.3	100.5	470.6	67.8	65.3	183.1	112.8	529.6	73.5	69.0	185.5	106.7	539.1
2011	53.5	52.9	153.2	107.4	461.9	60.5	63.1	179.5	120.3	522.1	63.0	65.6	175.7	107.5	511.0
2012	54.9	58.3	167.0	113.8	496.2	58.2	65.2	184.2	128.8	540.8	62.5	68.9	187.0	115.7	540.7
2013	54.3	62.6	160.4	120.9	503.0	56.7	68.8	171.2	131.3	532.2	61.8	73.8	176.8	114.6	531.5
2014	55.0	60.1	157.1	121.3	499.4	56.8	63.9	175.6	133.4	533.4	60.9	68.5	174.4	115.5	523.5
2015	55.1	61.4	145.1	115.6	484.7	56.8	66.9	159.0	130.4	520.2	59.5	69.3	160.5	109.2	504.3

888

Table 1. Annual total anthropogenic CO emission in different regions, from 2001 to 2015, constrained with MOPITT column, profile and lower tropospheric data. The region definition is shown in Figure 2e.

892

893

894

895

Years	MOPITT Column (Tg/year)					MOPITT Profile (Tg/year)					MOPITT Lower Profile (Tg/year)							
	Boreal North America	Boreal Asia	South America	Africa	SE Asia	Gobal Total	Boreal North America	Boreal Asia	South America	Africa	SE Asia	Gobal Total	Boreal North America	Boreal Asia	South America	Africa	SE Asia	Gobal Total
2001	1.2	24.8	25.5	160.8	14.0	272.4	1.2	26.5	28.4	153.5	9.5	267.7	1.3	28.4	31.9	222.0	21.4	369.6
2002	10.1	23.7	38.4	164.5	44.9	331.5	12.6	50.6	40.7	171.3	36.1	369.2	17.0	65.9	42.1	222.9	67.9	488.3
2003	8.9	47.7	39.6	162.7	17.2	324.2	11.1	65.4	41.4	174.9	14.1	356.2	13.6	76.9	44.0	220.9	24.8	445.2
2004	12.7	4.7	55.3	136.9	39.5	292.3	26.9	5.9	58.4	158.6	44.4	350.1	46.3	6.8	55.7	167.1	46.7	381.1
2005	11.2	7.7	61.8	167.4	29.4	318.4	15.5	9.8	67.3	193.3	31.1	364.9	19.1	11.3	68.1	203.1	34.8	387.3
2006	4.5	11.5	32.9	134.0	51.0	278.0	5.4	14.3	36.3	158.1	68.4	337.6	5.8	15.4	32.9	164.6	77.9	354.9
2007	5.1	10.2	72.9	154.9	19.3	313.4	5.9	12.8	84.6	174.3	23.9	365.8	6.6	13.8	78.4	182.1	23.7	369.3
2008	3.6	19.5	26.9	151.9	10.9	245.9	4.0	25.3	31.1	176.2	13.5	288.4	4.9	26.2	31.3	174.8	13.4	290.4
2009	5.4	11.1	16.4	132.8	36.7	254.8	5.7	12.8	16.9	142.2	37.3	274.1	6.1	13.2	16.8	139.5	38.3	274.2
2010	7.5	13.0	61.8	150.5	15.1	281.9	10.4	16.8	72.4	168.1	20.2	329.1	11.4	19.5	69.1	167.3	20.4	329.6
2011	4.1	13.3	15.1	145.7	11.5	240.3	5.1	15.8	16.6	153.0	15.4	261.5	5.6	16.1	16.3	145.4	13.4	250.8
2012	4.8	15.3	24.9	143.7	13.8	256.1	5.1	16.6	25.5	151.9	16.9	275.6	5.8	17.0	26.5	154.4	16.9	277.1
2013	4.5	11.7	12.4	172.0	13.1	257.6	6.0	12.9	13.9	170.8	22.7	270.1	6.7	13.8	16.0	187.0	14.6	284.4
2014	6.8	13.9	17.9	167.0	21.4	275.4	8.1	15.4	17.3	161.1	25.8	275.6	7.4	15.3	18.6	181.3	19.8	289.6
2015	7.0	14.3	29.3	193.6	66.4	357.7	7.4	15.3	28.0	188.9	162.0	448.1	6.8	14.3	28.1	204.0	87.1	386.5

896

Table 2. Annual total biomass burning CO emission in different regions, from 2001 to 2015, constrained with MOPITT column, profile and lower tropospheric data. The region definition is shown in Figure 2f.

900

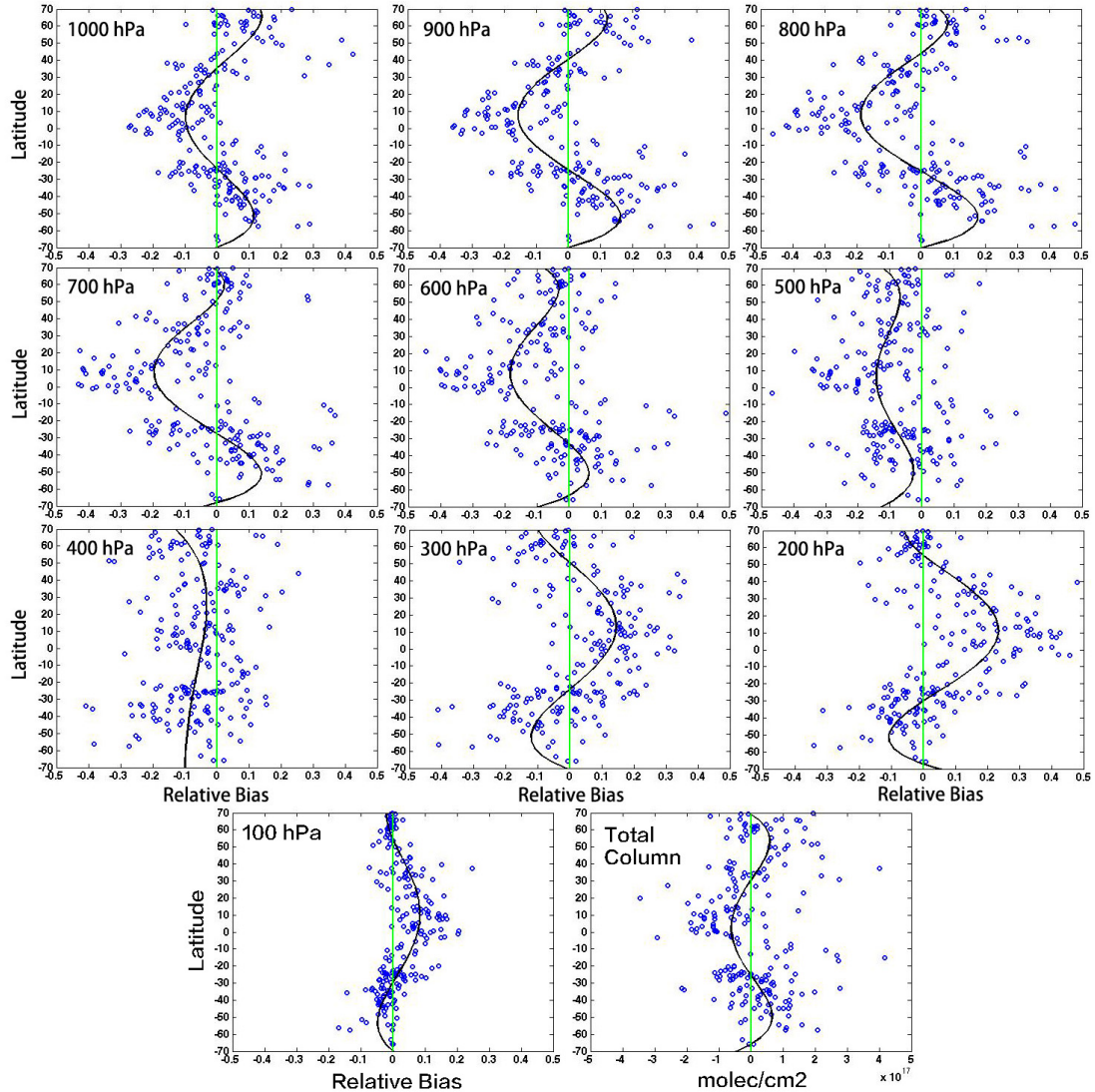
901

902

903

904

905
906
907
908
909
910
911



912
913
914
915
916
917
918
919
920
921
922

Figure 1. Difference between MOPITT CO retrievals and HIPPO aircraft measurements. The aircraft measurements are smoothed with MOPITT averaging kernels. The black solid line shows the 4-order polynomial curve fitting, which is used to correct MOPITT data in this work.

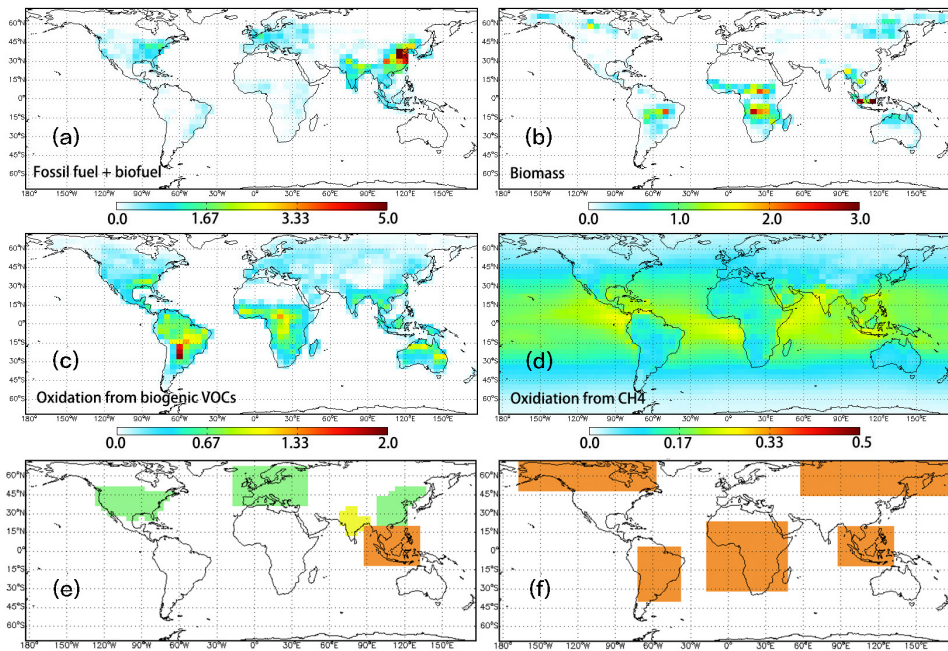


Figure 2. (a-d) Mean a priori CO emissions from combustion sources and the oxidation of biogenic VOCs and CH₄ from 2001 to 2015. The unit is 10¹² molec/cm²/sec. (e-f) Region definitions for (e) anthropogenic and (f) biomass burning sources.

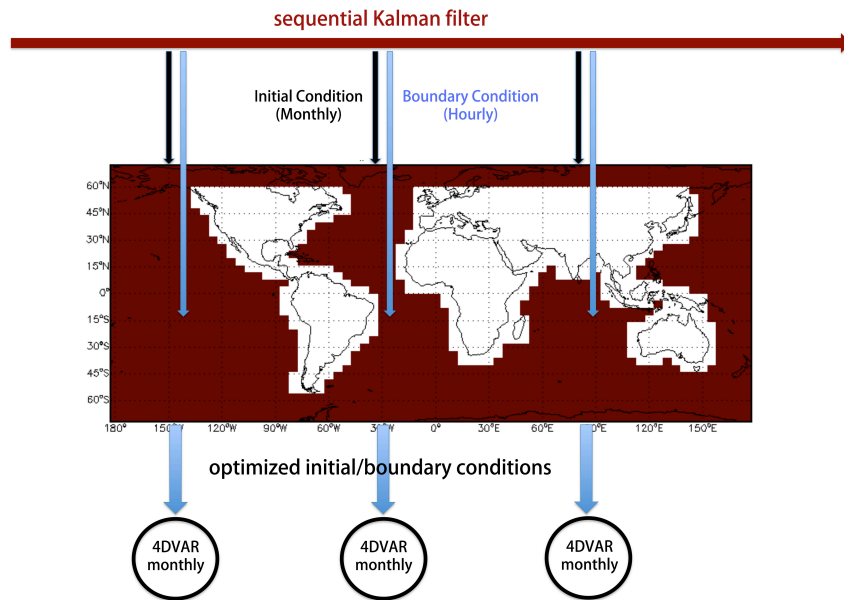
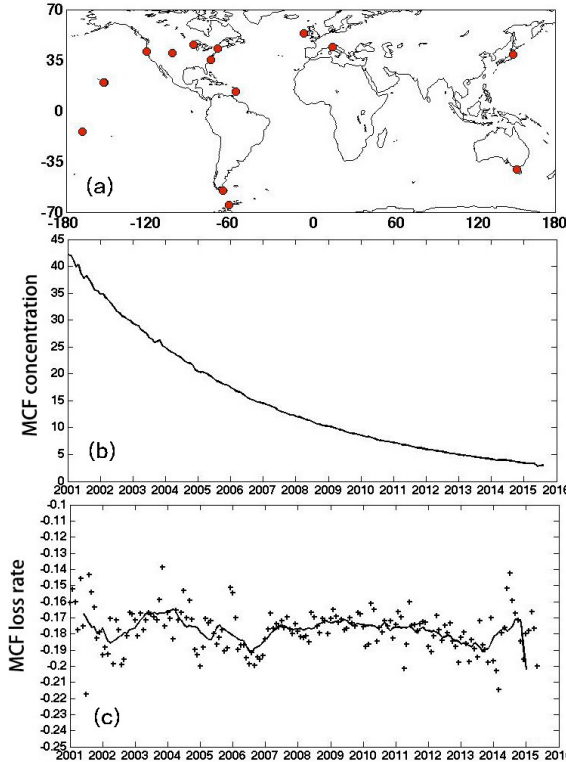
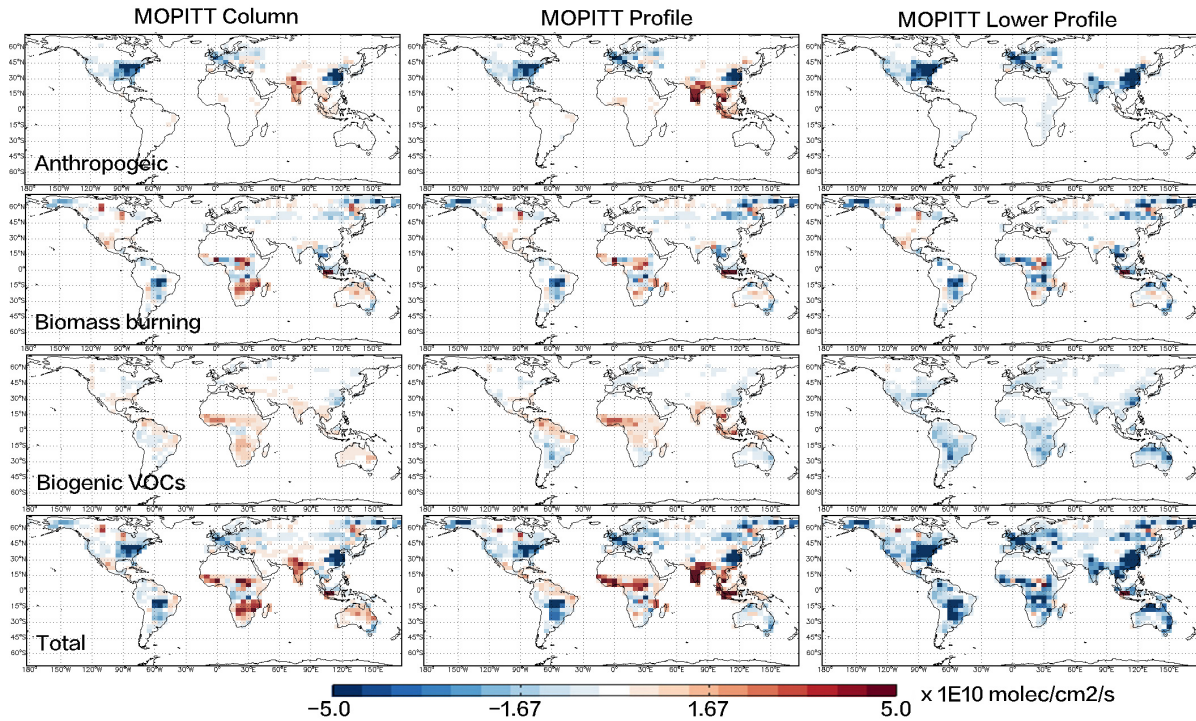


Figure 3. Schematic diagram for methodology of the assimilation system. Sequential Kalman Filter was run from March 1 2000 to December 31 2015 to produce the optimized initial conditions (monthly) and boundary conditions (hourly). Monthly 4-DVAR inversions were performed with the optimized initial conditions. Only MOPITT data over land (white grids) were assimilated in the 4-DVAR inversions, while the CO abundances over ocean (red grids) were defined as boundaries and rewritten using the optimized hourly CO fields from Kalman Filter. The Kalman filter run is completely independent of the 4-DVAR inversions. There is no feedback of the 4-DVAR inversion results to the boundary conditions.



936

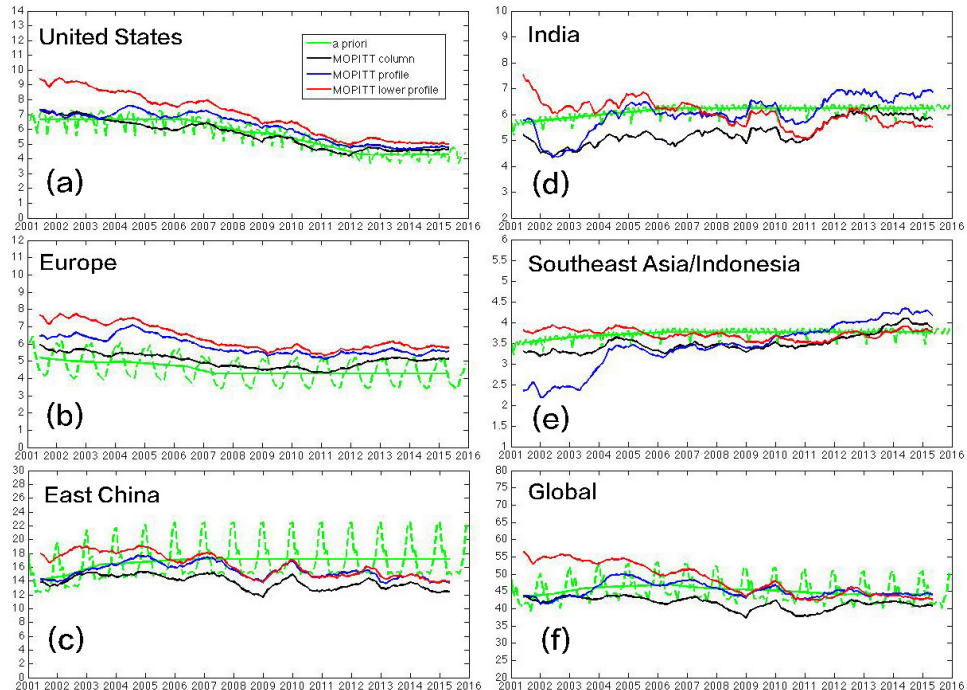
937 **Figure 4.** (a) Locations of WDCGG sites with MCF measurements. (b) Global mean MCF
 938 concentration. (c) Exponential loss rate of MCF, derived from 12-month apart of monthly
 939 means [e.g., $\ln(MCF_{Jan2007}/MCF_{Jan2006})$]. The black solid line shows the 12-month mean value.
 940



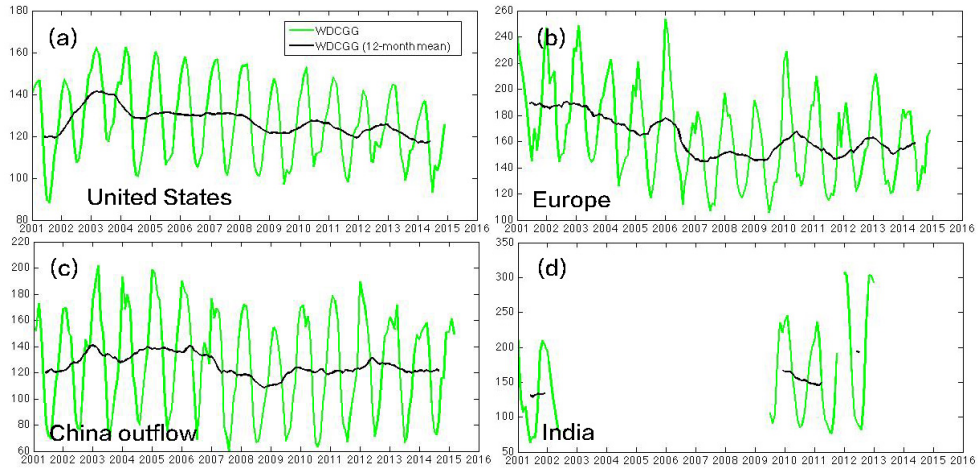
941

942 **Figure 5.** CO emission trends for 2001 – 2015, constrained with MOPITT column, profile and
 943 lower tropospheric profile data. The months dominated by biomass burning emissions are
 944 excluded from the trend calculation for anthropogenic and biogenic VOC emissions.

Anthropogenic Emissions

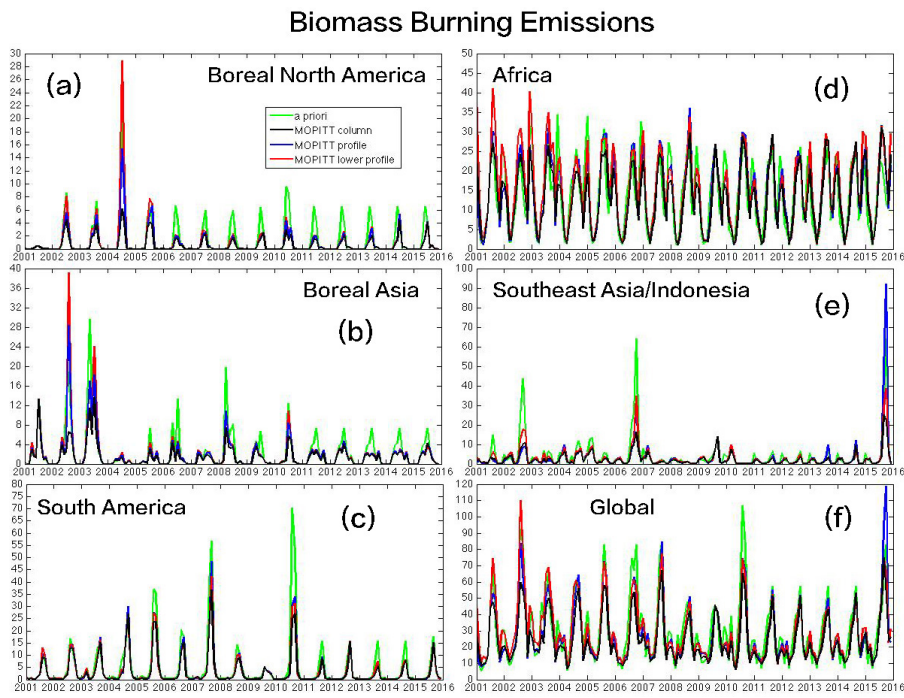


947 **Figure 6.** 12-month mean value of anthropogenic CO emissions (with unit Tg/month) for 2001
948 – 2015: a priori emission (green) and a posteriori emissions constrained with MOPITT column
949 data (black), MOPITT profile data (blue) and MOPITT lower tropospheric profile data (red).
950 The green dash line shows the monthly a priori anthropogenic CO emissions. The region
951 definition is shown in Figure 2e.



955 **Figure 7.** Monthly mean CO concentrations (green) and 12-month mean value (black) from
956 WDCGG stations for 2001 – 2015. (a) 15-station average in United States (b) 20-station
957 average in Europe (c) 2-station (YON and JMA) average in east China outflow (4) Cape Rama
958 (CRI) in India.

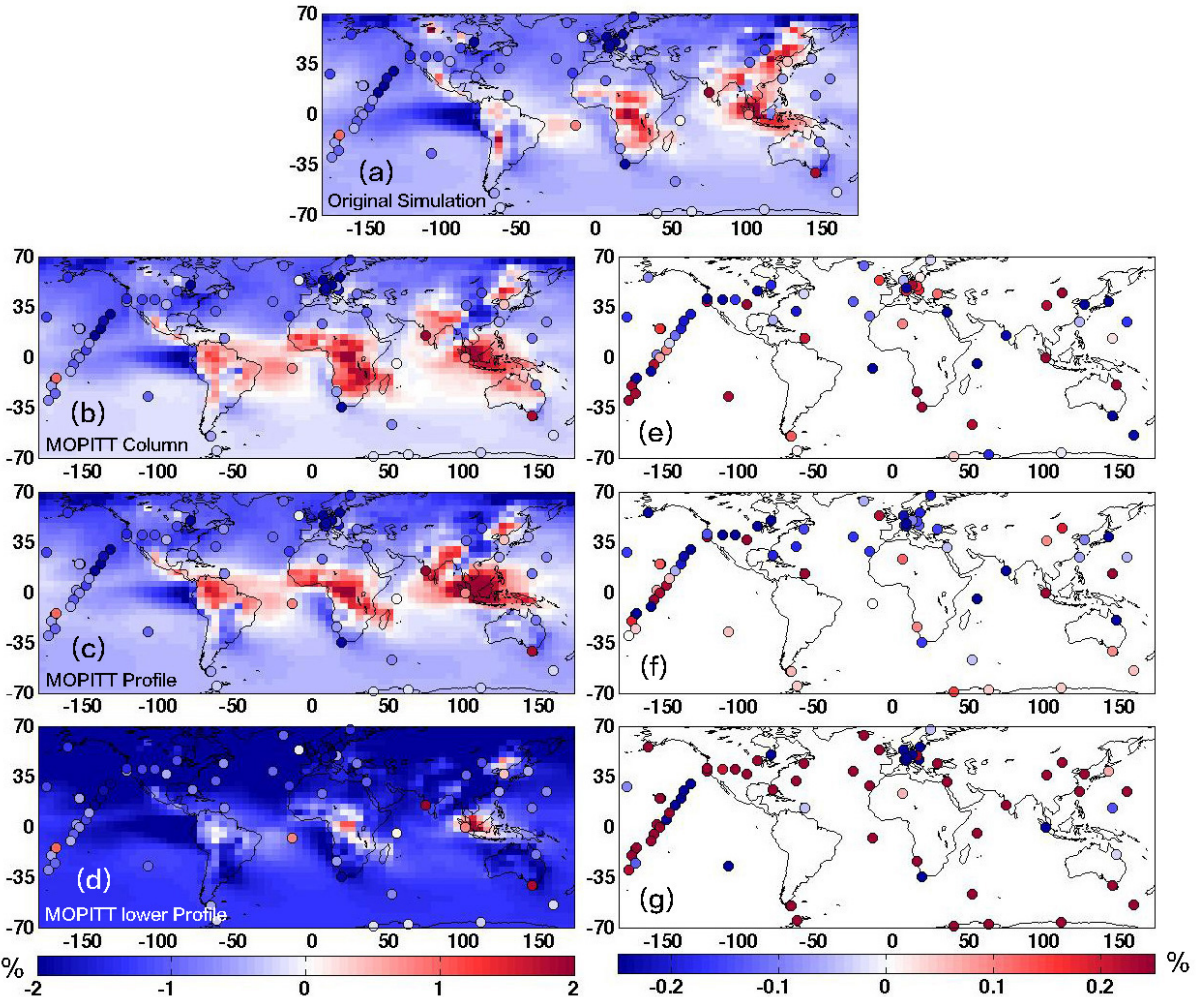
961
962
963
964
965
966
967
968
969
970
971
972



973
974
975
976
977
978
979
980
981
982
983
984
985
986
987
988

Figure 8. Monthly biomass burning CO emissions (with unit Tg/month) for 2001 – 2015: a priori emission (green) and a posteriori emissions constrained with MOPITT column data (black), MOPITT profile data (blue) and MOPITT lower tropospheric profile data (red). The region definition is shown in Figure 2f.

989
990
991
992
993

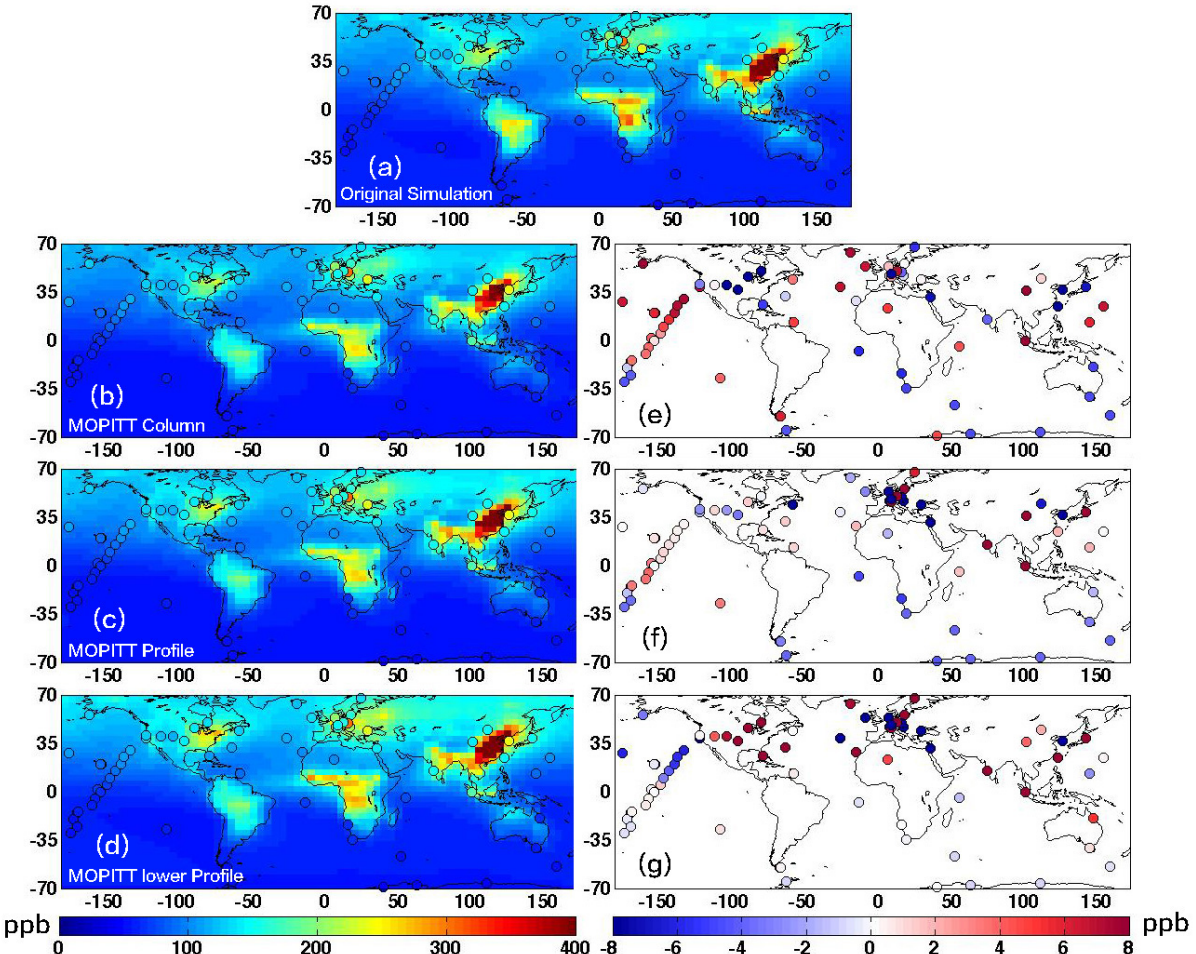


994

995 **Figure 9.** Panels (a-d): long-term trend (annual) of surface CO concentration for 2001 – 2015
996 from WDCGG sites, and model simulations driven with a priori and a posteriori emissions.
997 Panels (e-g): effect of a posteriori emissions, derived by $\text{abs}(\text{Trend}_{\text{a posteriori}} - \text{Trend}_{\text{WDCGG}}) -$
998 $\text{abs}(\text{Trend}_{\text{a priori}} - \text{Trend}_{\text{WDCGG}})$; blue (red) means the a posteriori emissions improves (degrades)
999 the agreement with WDCGG measurements compared to the a priori emissions, while white
1000 indicates no change from the priori. Only stations with more than 10 year observations (the
1001 time range between the first and last observations) during 2001-2015 are included.

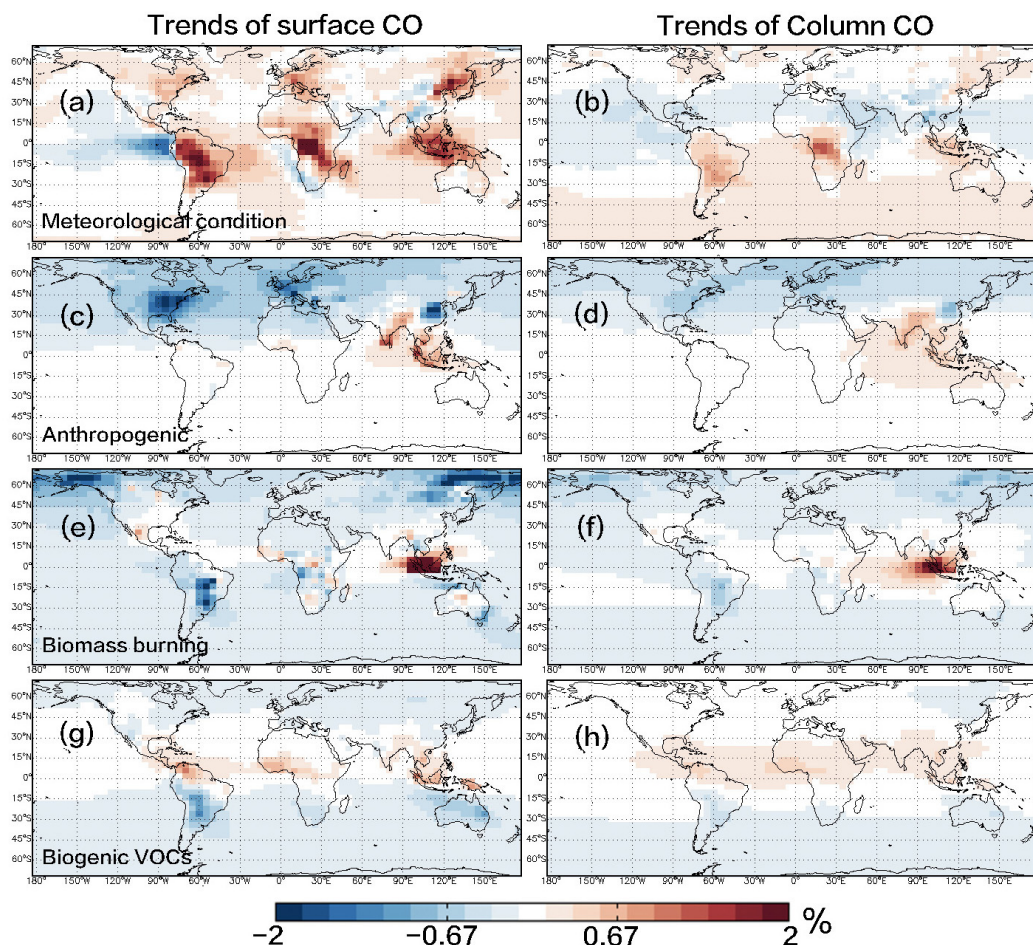
1002
1003
1004
1005
1006
1007
1008

1009
1010
1011
1012
1013



1014
1015 **Figure 10.** Panels (a-d): long-term mean value of surface CO concentration for 2001 – 2015
1016 from WDCGG sites, and model simulations driven with a priori and a posteriori emissions.
1017 Panels (e-g): effect of a posteriori emissions, derived by $\text{abs}(\text{CO}_{\text{aposteriori}} - \text{CO}_{\text{WDCGG}}) -$
1018 $\text{abs}(\text{CO}_{\text{apriori}} - \text{CO}_{\text{WDCGG}})$; blue (red) means the a posteriori emissions improves (degrades) the
1019 agreement with WDCGG measurements compared to the a priori emissions, while white
1020 indicates no change from the priori. Only stations with more than 10 year observations (the
1021 time range between the first and last observations) during 2001-2015 are included.
1022
1023
1024
1025
1026
1027
1028
1029

1030
1031
1032
1033
1034
1035
1036
1037



1038
1039
1040
1041
1042

Figure 11. Long-term trend (annual) of modeled surface and column CO for 2001 – 2015 with (a-b) all emission sources are fixed at 2001 level. (c-d) variable anthropogenic emissions; (e-f) variable biomass burning emissions; (g-h) variable biogenic VOCs emissions; The variable emissions are constrained with MOPITT profile data.